ACS APPLIED MATERIALS & INTERFACES

www.acsami.org

Research Article

# Microporous Metal–Organic Framework with a Completely Reversed Adsorption Relationship for $C_2$ Hydrocarbons at Room Temperature

Fang-Zhou Sun, Shan-Qing Yang, Rajamani Krishna, Ying-Hui Zhang, Yu-Pei Xia, and Tong-Liang Hu*

Cite This: *ACS Appl. Mater. Interfaces* 2020, 12, 6105–6111

Read Online

ACCESS | Metrics & More | Article Recommendations | Supporting Information

**ABSTRACT:** As a new type of porous material, metal–organic frameworks (MOFs) have been widely studied in gas adsorption and separation, especially in $C_2$ hydrocarbons. Considering the stronger interaction between the unsaturated molecules and the metal sites, and the smaller molecular size of unsaturated molecules, the usual relationship of affinities and adsorption capacities among $C_2$ hydrocarbons in most common MOFs is $C_2H_2 > C_2H_4 > C_2H_6$. Herein, a unique microporous metal–organic framework, **NUM-7a** (activated **NUM-7**), with a completely reversed adsorption relationship for $C_2$ hydrocarbons ($C_2H_6 > C_2H_4 > C_2H_2$) has been successfully synthesized, which breaks the traditional concept of the adsorption relationship of MOFs for $C_2$ hydrocarbons. Based on this unique adsorption relationship, a green and simple one-step separation purification for a large amount of $C_2H_4$ can be expected to be achieved through the selective adsorption of $C_2H_6$. In addition, **NUM-7a** also shows good selectivities in $C_2H_2/CO_2$ and $CO_2/CH_4$.

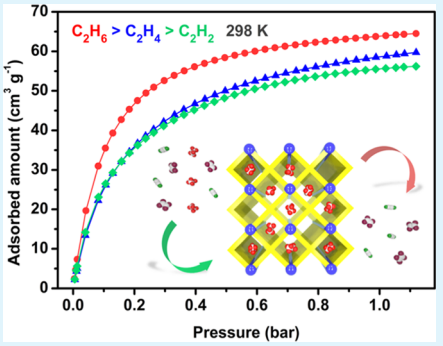


**KEYWORDS:** *metal–organic framework, microporous, $C_2$ hydrocarbons, reversed adsorption relationships, green and efficient one-step separation of $C_2H_4$ and $C_2H_6$*

Downloaded via UNIV AMSTERDAM on June 29, 2020 at 04:08:08 (UTC).
See https://pubs.acs.org/sharingguidelines for options on how to legitimately share published articles.

## INTRODUCTION

Separation and purification of $C_2$ hydrocarbons are very valuable, the products of which are the most important cornerstone of industrial production. $C_2$ hydrocarbon separation products that are regarded as the blood of the industry, with an annual output of hundreds of millions of tons,[1] are widely used in the further synthesis of various industrial products, which are ubiquitous in human life, such as fibers, plastics, rubber, and the likes.[2] Therefore, such high annual output is followed by an extremely high energy consumption problem, which is usually required to achieve high-temperature and high-pressure conditions for the separations of light hydrocarbons with exceptionally similar physical and chemical characteristics.[1] Nowadays, with the increasingly serious energy and environmental issues, energy conservation and emission reduction in all fields urgently need more attention. More efficient and energy-efficient separation methods need to be found to replace the traditional high-energy cryogenic rectification methods.

Metal–organic frameworks (MOFs), as a new type of remarkable porous material with extremely high surface area, structural tenability, linkers tailorability, and controllable properties,[3] have been widely used in pressure swing adsorption (PSA), which is an efficient separation method with simple operation, high product purity, and low energy consumption.[4] Especially in the separation of light hydrocarbons, MOFs are considered to be a kind of green separation material with great potential and bright prospects, which are widely studied by many researchers.[5−17] Up to now, many types of MOFs have been reported to have good performance in $C_2H_4/C_2H_6$[5,6,9,18−20] and $C_2H_2/C_2H_4$[5,7−9,13−15,21] separations. Typically, due to the stronger interaction between the unsaturated molecules and the metal sites, and the smaller molecule size of unsaturated molecules resulting in more molecules being captured by the framework, the usual relationship of affinities and adsorption capacities among $C_2$ hydrocarbons in most common MOFs is $C_2H_2 > C_2H_4 > C_2H_6$.[5,6] In the separation of $C_2H_4/C_2H_6$ mixture, which accounts for the majority of $C_2$ hydrocarbons separation with a great energy consumption, because of the interaction relationship of $C_2$ hydrocarbons with frameworks, most MOFs selectively adsorb $C_2H_4$ and then obtain a purified $C_2H_4$ product by further desorption and subsequent series of steps.[1] As a result, the process of $C_2H_4$ purification and energy consumption still needs to be optimized. Fortunately, some MOFs with partially reversed adsorption characteristics ($C_2H_6 > C_2H_4$) have been reported in recent years, which can directly obtain purified $C_2H_4$ by the selective adsorption of

Received: December 11, 2019
Accepted: January 10, 2020
Published: January 10, 2020


© 2020 American Chemical Society

https://dx.doi.org/10.1021/acsami.9b22410
*ACS Appl. Mater. Interfaces* 2020, 12, 6105–6111

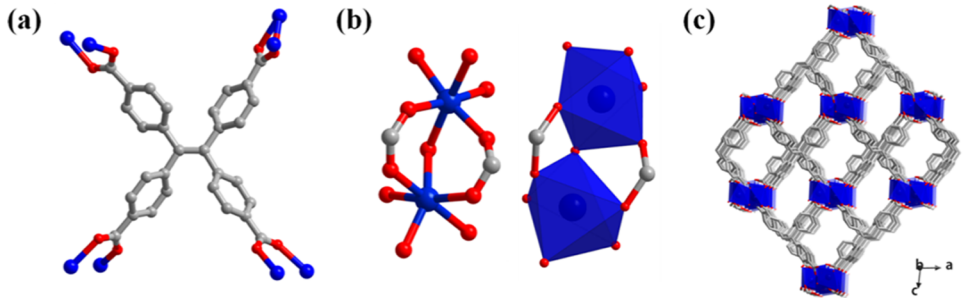


**Figure 1.** X-ray single-crystal structure of **NUM-7**, indicating (a) the coordination model of each organic ligand $TCPE^{4-}$ and (b) the coordination environments of Mn(II) ions in a binuclear manganese SBU; and (c) the three-dimensional framework with one-dimensional channels along *b*-axis. Mn, O, and C are represented by blue, red and gray, respectively.

$C_2H_6$ through the reversed affinity and adsorption capacity of the frameworks to the $C_2H_6/C_2H_4$ mixture.[22−26] As a simple, efficient, and green adsorbent, this type of MOFs with reversed adsorption characteristics is in line with the current global energy saving and emission reduction trend, so it is worth exploring further.

Herein, inspired by the fascinating characteristics of selective adsorption of alkane, we construct a microporous MOF, **NUM-7**, with one-dimensional (1D) channels having completely reversed selectivity for $C_2$ hydrocarbons through selecting a tetra-carboxylate ligand. Unlike the traditional impression of the interaction between MOFs and $C_2$ hydrocarbons, **NUM-7a** (the activated **NUM-7**) exhibits a unique and strong affinity for $C_2H_6$ with a completely reversed relationship of affinities and adsorption capacities among $C_2$ hydrocarbons ($C_2H_6 > C_2H_4 > C_2H_2$). Since the content of $C_2H_4$ in the product obtained by $C_2H_6$ cracking can reach several to several tens of times that of $C_2H_6$, the requirement for adsorption capacity to obtain equal amount of purified ethylene can be largely reduced for $C_2H_6$-selectivity MOFs, which means that it is expected that two relatively contradictory properties of high selectivity and high adsorption capacity in $C_2H_4$-selectivity MOFs will be realized simultaneously by $C_2H_6$-selectivity MOFs. Based on the unique reversed relationship of the adsorption capacities of the framework for $C_2$ hydrocarbons, a one-step greener purification of $C_2H_4$ can be achieved through the selective adsorption of $C_2H_6$ with the energy consumption decreasing by 40% in industrial separation, which omitted the desorption process compared to the MOFs with $C_2H_4$-selectivity.[22]

## EXPERIMENTAL SECTION

**Materials and Methods.** All of the reagents and solvents were purchased from commercial suppliers and used without further purification. Powder X-ray diffraction (PXRD) and variable temperature powder X-ray diffraction (VT-PXRD) data were collected on a Rigaku Miniflex 600 at 40 kV and 15 mA with a scan rate of 6.0° $min^{-1}$ using Cu K$\alpha$ radiation in an air atmosphere ($3° \le 2\theta \le 60°$). Thermogravimetric analysis (TGA) studies were carried out on a Rigaku standard thermogravimetry−differential thermal analysis (TG−DTA) analyzer from room temperature to 800 °C under air atmosphere with a heating rate of 10 °C $min^{-1}$, using an empty and clean $Al_2O_3$ crucible as a reference.

**Synthesis of NUM-7.** A mixture of $MnCl_2{\cdot}4H_2O$ (0.1 mmol, 0.020 g) and $H_4TCPE$ (0.01 mmol, 10 mg, $H_4TCPE$ = 4,4′,4″,4‴-(ethene-1,1,2,2-tetrayl) tetrabenzoic acid) was dissolved by dimethylformamide (DMF) (1.5 mL), $CH_3CN$ (1 mL), and deionized water (0.25 mL) in a 10 mL screw-capped glass vial, and then the sealed vial was heated to 85 °C for 72 h, which was then cooled to room temperature. The light yellow stick crystals obtained were washed several times with DMF for single-crystal X-ray diffraction analysis. Yield: about 93% based on $H_4TCPE$.

**Activation of NUM-7.** The as-synthesized **NUM-7** was washed several times with DMF. Whereafter, fast and frequent guest solvents are exchanged for 6 h using absolute methanol to replace the DMF and $CH_3CN$ solvent molecules in the channels. After filtering, the guest-exchanged **NUM-7** was activated at 150 °C for 10 h under vacuum conditions (less than $10^{-5}$ Torr), giving **NUM-7a**.

**Gas Sorption Measurements.** $N_2$ adsorption−desorption isotherms from 0 to 1 bar at 77 K with liquid nitrogen were measured by a Micrometrics ASAP 2460 volumetric gas adsorption analyzer. The measurements of gas adsorption of hydrocarbons from 273 to 313 K precisely controlled through a LAUDR RP890 recirculating control system with absolute ethyl alcohol were carried out by a Micrometrics ASAP 2020M volumetric gas adsorption analyzer.

**Crystallography.** The single-crystal X-ray diffraction data of **NUM-7** were collected on a Rigaku XtaLAB Pro MM007HF DW diffractometer at 100 K with Cu K$\alpha$ radiation ($\lambda$ = 1.54184 Å) by scan mode. The structure was solved and refined by the full-matrix least-squares method through Olex2 software[27] with the SHELXT[28] and SHELXL[29] program, respectively. The details have been listed in Table S1, and the crystallographic data have been deposited in the Cambridge Crystallographic Data Center (CCDC number 1951489). The CIF file can be obtained conveniently from the website: https://www.ccdc.cam.ac.uk/structures.

## RESULTS AND DISCUSSION

**Single-Crystal X-ray Structure.** The single crystals of **NUM-7** ($[Mn_2(TCPE)(DMF)(H_2O)]{\cdot}(DMF)(CH_3CN)$) were obtained using a simple and convenient one-pot solvothermal reaction of manganese chloride tetrahydrate ($MnCl_2{\cdot}4H_2O$) and $H_4TCPE$ in a DMF/$CH_3CN$ mixture solvent. Single-crystal X-ray diffraction revealed that **NUM-7** is in the clinorhombic crystal group with the $P2_1/c$ space group (more details of the crystal structure are shown in Table S1). The asymmetric unit of **NUM-7** contains one complete 4-connected ligand ($TCPE^{4-}$) (Figure 1a), two independent but different hexacoordinated Mn(II) ions and two more solvent molecules (a DMF molecule and an $H_2O$ molecule), which coordinated with two Mn(II) ions, respectively (Figure S1). Also, each pair of different hexacoordinated Mn(II) ions construct a dual-core secondary building unit (SBU) connected by three carboxyl groups (Figure 1b), with two carboxyl groups adopting a bidentate bridging mode and one adopting a bidentate 1,3-chelating mode. The repeated 6-connected dual-core SBUs form the infinitely extendable Mn−O chain SBU by sharing oxygen atoms from DMF molecules and carboxyl groups, respectively. The overall three-dimensional (3D) structure in a shape of a fence is constructed by ligands and SBU chains, which has narrow approximated


https://dx.doi.org/10.1021/acsami.9b22410
ACS Appl. Mater. Interfaces 2020, 12, 6105−6111

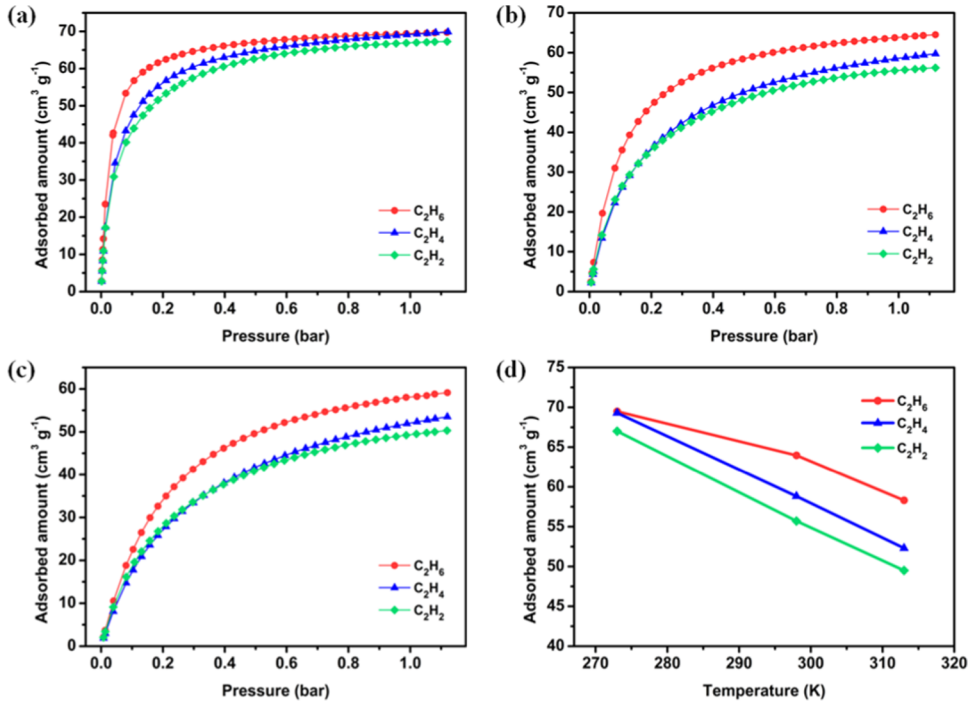


**Figure 2.** Single-component adsorption isotherms for $C_2H_6$ (red), $C_2H_4$ (blue), and $C_2H_2$ (green) for **NUM-7a** at (a) 273 K, (b) 298 K, and (c) 313 K. (d) Trends of adsorption capacities of $C_2H_6$, $C_2H_4$, and $C_2H_2$ with the change of temperature.

rectangular 1D channels with a scale of about 4.7 × 7.8 Å$^2$ along *b*-axis built by multiple rotatable phenyl rings.

**Stabilities of NUM-7.** The stabilities of **NUM-7** were demonstrated by PXRD and TGA. The PXRD patterns indicate that **NUM-7** can remain stable in most common solvents (Figure S2). As shown in Figures S3 and S4, TGA and VT-PXRD show that the structure of **NUM-7** can be maintained to at least 160 °C, and with the increase of temperature, the framework changed and eventually collapsed at about 400 °C. In addition, the crystalline feature of **NUM-7** can also be maintained after removing the solvents in the pore (Figure S5). It can be seen that **NUM-7** has excellent stability, which is vital for its subsequent applications in adsorption and separation.

**Reversed Gas Sorption Properties of NUM-7a.** $N_2$-gas adsorption and desorption curves of **NUM-7a** at 77 K were measured to assess the permanent porosity. As shown in Figure S6, the fully reversible type I isotherm with a sharp uptake at $P/P_0 < 0.05$ reveals the microporous nature of **NUM-7a**. The $N_2$-gas physisorption reached a balanced plateau at $P/P_0 > 0.05$, with a saturation uptake of 125.9 cm$^3$ g$^{-1}$. According to the measured $N_2$ adsorption results, the Brunauer–Emmett–Teller (Langmuir) surface area of **NUM-7a** is 345 m$^2$ g$^{-1}$ (526 m$^2$ g$^{-1}$), and pore volume is 0.194 cm$^3$ g$^{-1}$, obtained by calculation. The aperture of 1D channels in **NUM-7a** is about 3.42 Å, obtained by the Horvath–Kawazoe method (Figure S7).

Exactly as the pre-expectation of the designed structure, **NUM-7a** has 1D narrow channels with a faceted hole wall made up of many phenyl rings, which portends that the framework is expected to have a stronger host–guest interaction with $C_2H_6$.[30−32] So, the $C_2$ hydrocarbons single-component adsorption isotherms of **NUM-7a** were measured at 273, 298, and 313 K, respectively. The adsorption isotherms of $C_2$ hydrocarbons from 273 to 313 K with pressure up to 1 bar were investigated as shown in Figure 2. A peculiar whole reversed adsorption phenomenon of $C_2$ hydrocarbons was observed, which broke our normal cognition about the relationship among $C_2$ hydrocarbons. At 273 K, although the adsorption capacities at 1 bar of $C_2H_6$ (69.5 cm$^3$ g$^{-1}$), $C_2H_4$ (69.3 cm$^3$ g$^{-1}$), and $C_2H_2$ (67.0 cm$^3$ g$^{-1}$) are abnormally close, a steeper rising trend in the type I curve of $C_2H_6$ compared to $C_2H_4$ and $C_2H_2$ can be observed from 0 to 0.2 bar in Figure 2a–c, which indicates that $C_2H_6$ has a stronger host–guest interaction with **NUM-7a**. As the temperature increases, this unique reversed adsorption phenomenon is amplified. At 298 K, the adsorption capacity of $C_2H_6$ (63.9 cm$^3$ g$^{-1}$) is significantly higher than that of $C_2H_4$ (58.6 cm$^3$ g$^{-1}$) and $C_2H_2$ (55.5 cm$^3$ g$^{-1}$) while maintaining a steeper curve rising trend of $C_2H_6$ than $C_2H_4$ and $C_2H_2$ in the low-pressure region. As the temperature rises further to 313 K, the relationship between the adsorption curves remains consistent with that at 298 K despite a slight decrease in adsorption capacities of $C_2H_6$ (58.1 cm$^3$ g$^{-1}$), $C_2H_4$ (52.1 cm$^3$ g$^{-1}$), and $C_2H_2$ (49.4 cm$^3$ g$^{-1}$). In general, as the temperature increases, the saturated adsorption capacity of each component decreases, but the difference between the three components is gradually amplified, as shown in Figure 2d. Comparison of some other gases adsorption curves, as shown in Figures S8–S11, **NUM-7a** exhibits significant differences in its adsorption capacities for $C_2H_2$, $CO_2$, and $CH_4$. For $C_2H_2$ and $CO_2$, the difference in adsorption curves is very obvious in the low-pressure region. The curve of $C_2H_2$ is significantly steeper than that of $CO_2$, and about 75% of the adsorption capacity is filled in 0–0.1 bar, which indicates that $C_2H_2$ has a stronger interaction with the framework than $CO_2$. Also, for $CO_2$ and $CH_4$, the $CO_2$ adsorption capacity is more than double that of $CH_4$, and the curve of $CH_4$ rises very gently with increasing pressure, which shows a weak affinity between $CH_4$ and framework.


https://dx.doi.org/10.1021/acsami.9b22410
ACS Appl. Mater. Interfaces 2020, 12, 6105−6111

Considering the above factors, **NUM-7a** has potential in the separation of $C_2H_2/CO_2$ and $CO_2/CH_4$.

Considering the above uncommon phenomena, the coverage-dependent adsorption enthalpies ($Q_{st}$) of **NUM-7a** for $C_2H_6$, $C_2H_4$, and $C_2H_2$ were evaluated experimentally from single-component isotherms by the implementation of a virial equation (Figures 3 and S12–S14). The resultant $Q_{st}$

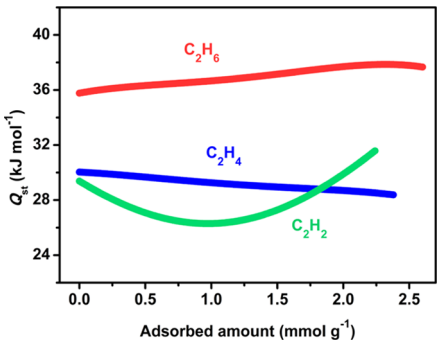


**Figure 3.** $Q_{st}$ relationship of $C_2H_6$ (red), $C_2H_4$ (blue), and $C_2H_2$ (green) adsorption for **NUM-7a** estimated from virial expression fits at 298 and 313 K.

relationship at zero coverage among $C_2H_6$ (35.8 kJ $mol^{-1}$), $C_2H_4$ (30.0 kJ $mol^{-1}$), and $C_2H_2$ (29.3 kJ $mol^{-1}$) is indeed in good agreement with the unique reversed adsorption phenomenon previously seen. Moreover, with the increase of coverage, the interaction between $C_2H_4$ and the framework gradually decreases, and the adsorption enthalpy shows a slight downward trend. However, due to the interaction between guest molecules, the adsorption enthalpy of $C_2H_6$ shows an upward trend with the increase in adsorption amount. The difference in affinity between $C_2H_6/C_2H_4$ and **NUM-7a** is amplified due to the above changes in adsorption enthalpies, which is advantageous for the challenging and rewarding $C_2H_6/C_2H_4$ separation.

To structurally understand this kind of reversed strength of host–guest interactions, the distribution of $C_2$ hydrocarbons molecules in **NUM-7a** at 298 K and 1 bar had been confirmed by grand canonical Monte Carlo (GCMC) simulation.[33,34] The calculation results indicated that the host–guest interaction strength relationship between $C_2$ hydrocarbons and the framework is indeed $C_2H_6 > C_2H_4 > C_2H_2$ (Figures 4 and S15–S18). Also, the reason why the $C_2$ hydrocarbons can have such a strong force with the framework is that the existence of C–H···O and C–H···$\pi$ interactions between guests and hosts. As shown in Figure 4a, $C_2H_6$ molecule has the largest size and the most complex 3D configuration in $C_2$ hydrocarbons, and it can interact more strongly with the microporous channel walls through C–H···O (H···O2, 2.50 Å < 2.72 Å, the sum of van der Waals radii of oxygen (1.52 Å) and hydrogen (1.20 Å) atoms) and C–H···$\pi$ (H···$\pi$, 2.84–3.68 Å) interactions. Due to the planar configuration of $C_2H_4$ and the smaller molecular size, fewer hydrogen atoms can only form weaker interactions with the surrounding oxygen and benzene rings (C–H···O2, 2.56 Å < 2.72 Å, C–H···$\pi$, 3.07–4.05 Å), as shown in Figure 4b. In view of the above results, the linear $C_2H_2$ molecule and the framework obviously have the weakest interaction, even the smallest C–H···O (H···O4, 2.77 Å) distance exceeded the sum of the van der Waals radii of hydrogen and oxygen atoms, and the weak C–H···$\pi$ (H···$\pi$, 3.59–4.60 Å) interaction becomes weaker than that of $C_2H_6$ and $C_2H_4$. According to the above calculation results, it is precisely because of the difference in molecular size and spatial configuration that the molecule, which has more hydrogen atoms and large size, can form stronger interactions with the channel walls, resulting in the formation of a complete reversed affinity for the $C_2$ hydrocarbons.

**Evaluation of Separation Performance.** Based on this unique affinity reversed relationship of **NUM-7a**, the adsorption selectivity of binary mixtures $C_2H_6/C_2H_4$ in ratios of 50/50 (v/v) and 10/90 (v/v) at 298 K (Figure 5) and some

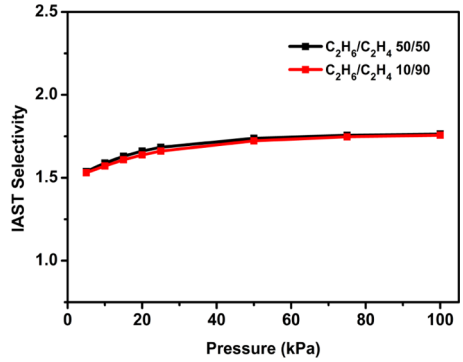


**Figure 5.** IAST selectivities of $C_2H_6/C_2H_4$ mixtures (50/50 and 10/90, v/v) for **NUM-7a** at 298 K.

other binary mixture gases (Figures S19–S27) were evaluated by ideal adsorbed solution theory (IAST). The estimated

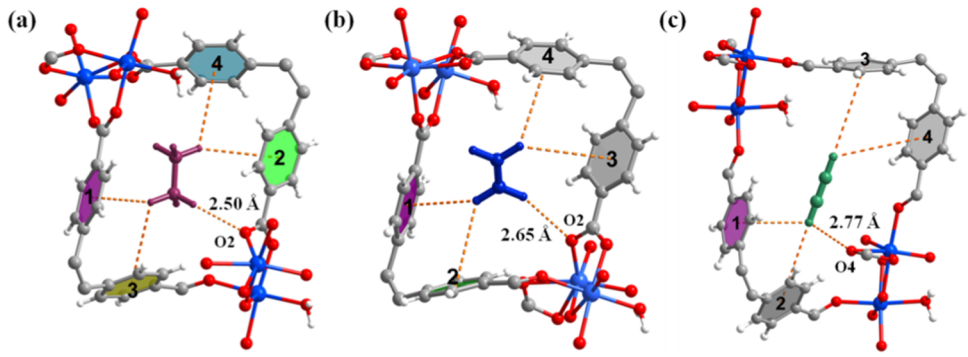


**Figure 4.** Results of the GCMC simulations, showing the adsorption sites for (a) $C_2H_6$, (b) $C_2H_4$, and (c) $C_2H_2$ in **NUM-7a**. The serial numbers of the benzene rings are determined according to the distance from benzene rings to the hydrogen atom on the guest molecules, and the distance of gray benzene rings to the nearest guest molecules is over 4.00 Å.



https://dx.doi.org/10.1021/acsami.9b22410
ACS Appl. Mater. Interfaces 2020, 12, 6105–6111

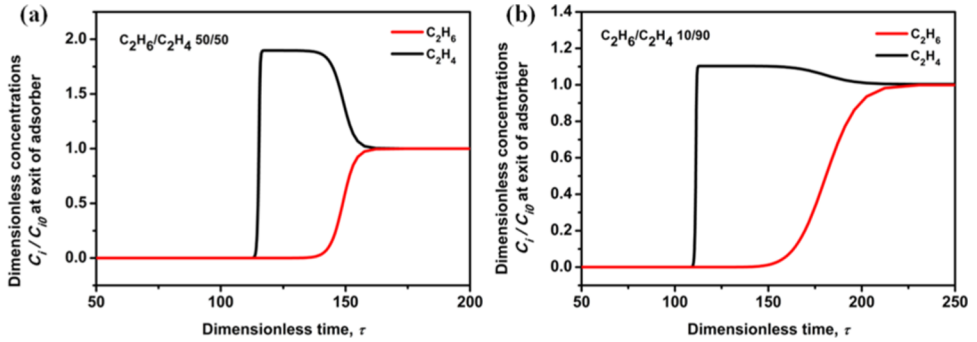


**Figure 6.** Transient breakthrough curves of (a) 50/50 and (b) 10/90 $C_2H_6/C_2H_4$ mixture in an adsorber bed packed with **NUM-7a** at total pressures of 100 kPa and 298 K. For the breakthrough simulations, the following parameter values were used, $L$ = 0.3 m; $\varepsilon$ = 0.4; $u$ = 0.04 m $s^{-1}$.

selectivities of **NUM-7a** for $C_2H_6/C_2H_4$ at 298 K and 1 bar are 1.764 and 1.757 in 50/50 and 10/90, respectively. Among the reported MOFs, the selectivity of **NUM-7a** at 298 K and 1 bar in 50/50 is higher than that of most $C_2H_6$-selectivity MOFs, which is higher than that of ZJU-30 (1.7),[36] ZIF-7 (1.5),[37] UTSA-33 (1.4),[38] and so forth (Table S3),[24,30,32,35,39,40] but lower than that of Fe($O_2$)dobdc (4.25),[22] Cu(Qc)$_2$ (3.4),[41] and MUF-15 (1.95).[25] The selectivities of $C_2H_2/CO_2$ and $CO_2/CH_4$ are as shown in Figures S26 and S27.

Building on above results, the separation performance of **NUM-7a** for $C_2H_6/C_2H_4$ (50/50 and 10/90) has been evaluated through breakthrough simulation experiment at 298 K. The transient breakthrough simulations show the concentrations of $C_2H_6/C_2H_4$ exiting the adsorber packed with **NUM-7a** as a function of the dimensionless time, $\tau$ (Figure 6). The breakthrough simulations demonstrate the potential of producing nearly pure product gas $C_2H_4$ during the time interval $\Delta\tau$ for both 50/50 and 10/90 $C_2H_6/C_2H_4$ mixtures, which indicates that **NUM-7a** has potential application in the challenging separation of $C_2H_6/C_2H_4$ in practice.

## CONCLUSIONS

We have developed a new microporous MOF (**NUM-7a**) showing a stronger affinity for $C_2H_6$ among $C_2$ hydrocarbons by selecting a small multibenzene ring ligand. **NUM-7a** exhibits an infrequent completely reversed adsorption relationship for $C_2$ hydrocarbons ($C_2H_6 > C_2H_4 > C_2H_2$) at the same condition, which breaks the traditional concept of adsorption relationship of MOFs for $C_2$ hydrocarbons. Based on this reversed adsorption phenomenon, the potential of **NUM-7a** in the separation of $C_2H_6/C_2H_4$ had been studied. The results demonstrated that $C_2H_4$ is expected to be directly and efficiently purified by a one-step green process through $C_2H_6$-selectivity **NUM-7a**.

## ASSOCIATED CONTENT

### Supporting Information

The Supporting Information is available free of charge at https://pubs.acs.org/doi/10.1021/acsami.9b22410.

Full experimental details, including crystal data, crystal structure, PXRD patterns, TGA curves, adsorption data, and grand canonical Monte Carlo (GCMC) simulations (PDF)

Data_NUM-7; symmetry employed for this SHELXL refinement; empirical absorption correction using spherical harmonics, implemented in SCALE3 ABSPACK scaling algorithm (CIF)

Structure factors for datablock(s) **NUM-7** (PDF)

## AUTHOR INFORMATION


### Corresponding Author

**Tong-Liang Hu** − *School of Materials Science and Engineering and Tianjin Key Lab for Rare Earth Materials and Applications, and Key Laboratory of Advanced Energy Material Chemistry (Ministry of Education), Nankai University, Tianjin 300350, China;* orcid.org/0000-0001-9619-9867; Email: tlhu@nankai.edu.cn

### Authors

**Fang-Zhou Sun** − *School of Materials Science and Engineering, Nankai University, Tianjin 300350, China*

**Shan-Qing Yang** − *School of Materials Science and Engineering, Nankai University, Tianjin 300350, China*

**Rajamani Krishna** − *Van 't Hoff Institute for Molecular Sciences, University of Amsterdam, Amsterdam 1098 XH, The Netherlands;* orcid.org/0000-0002-4784-8530

**Ying-Hui Zhang** − *School of Materials Science and Engineering and Tianjin Key Lab for Rare Earth Materials and Applications, and Key Laboratory of Advanced Energy Material Chemistry (Ministry of Education), Nankai University, Tianjin 300350, China*

**Yu-Pei Xia** − *School of Materials Science and Engineering, Nankai University, Tianjin 300350, China*

Complete contact information is available at: https://pubs.acs.org/10.1021/acsami.9b22410


### Notes

The authors declare no competing financial interest.

## ACKNOWLEDGMENTS

This work was financially supported by the NSFC (21673120) and the Fundamental Research Funds for the Central Universities, Nankai University (63196005).

## REFERENCES

(1) Sholl, D. S.; Lively, R. P. Seven Chemical Separations to Change the World. *Nature* **2016**, *532*, 435−437.

(2) Ren, T.; Patel, M.; Blok, K. Olefins from Conventional and Heavy Feedstocks: Energy Use in Steam Cracking and Alternative Processes. *Energy* **2006**, *31*, 425−451.

(3) Cui, W.-G.; Hu, T.-L.; Bu, X.-H. Metal-Organic Framework Materials for the Separation and Purification of Light Hydrocarbons. *Adv. Mater.* **2019**, No. 1806445.

(4) Mersmann, A.; Fill, B.; Hartmann, R.; Maurer, S. The Potential of Energy Saving by Gas-Phase Adsorption Processes. *Chem. Eng. Technol.* **2000**, *23*, 937−944.
(5) Bloch, E. D.; Queen, W. L.; Krishna, R.; Zadrozny, J. M.; Brown, C. M.; Long, J. R. Hydrocarbon Separations in a Metal-Organic Framework with Open Iron(II) Coordination Sites. *Science* **2012**, *335*, 1606−1610.
(6) Yang, S.; Ramirez-Cuesta, A. J.; Newby, R.; Garcia-Sakai, V.; Manuel, P.; Callear, S. K.; Campbell, S. I.; Tang, C. C.; Schröder, M. Supramolecular Binding and Separation of Hydrocarbons within a Functionalized Porous Metal-Organic Framework. *Nat. Chem.* **2015**, *7*, 121−129.
(7) Hu, T.-L.; Wang, H.; Li, B.; Krishna, R.; Wu, H.; Zhou, W.; Zhao, Y.; Han, Y.; Wang, X.; Zhu, W.; Yao, Z.; Xiang, S.; Chen, B. Microporous Metal-Organic Framework with Dual Functionalities for Highly Efficient Removal of Acetylene from Ethylene/Acetylene Mixtures. *Nat. Commun.* **2015**, *6*, No. 7328.
(8) Peng, Y.-L.; Pham, T.; Li, P.; Wang, T.; Chen, Y.; Chen, K.-J.; Forrest, K. A.; Space, B.; Cheng, P.; Zaworotko, M. J.; Zhang, Z. Robust Ultramicroporous Metal-Organic Frameworks with Benchmark Affinity for Acetylene. *Angew. Chem., Int. Ed.* **2018**, *57*, 10971−10975.
(9) Li, L. Y.; Guo, L. D.; Pu, S. Y.; Wang, J. W.; Yang, Q. W.; Zhang, Z. G.; Yang, Y. W.; Ren, Q. L.; Alnemrat, S.; Bao, Z. B. A Calcium-Based Microporous Metal-Organic Framework for Efficient Adsorption Separation of Light Hydrocarbons. *Chem. Eng. J.* **2019**, *358*, 446−455.
(10) Moreau, F.; da Silva, I.; Al Smail, N. H.; Easun, T. L.; Savage, M.; Godfrey, H. G. W.; Parker, S. F.; Manuel, P.; Yang, S.; Schröder, M. Unravelling Exceptional Acetylene and Carbon Dioxide Adsorption within a Tetra-Amide Functionalized Metal-Organic Framework. *Nat. Commun.* **2017**, *8*, No. 14085.
(11) Sapchenko, S. A.; Dybtsev, D. N.; Samsonenko, D. G.; Belosludov, R. V.; Belosludov, V. R.; Kawazoe, Y.; Schröder, M.; Fedin, V. P. Selective Gas Adsorption in Microporous Metal-Organic Frameworks Incorporating Urotropine Basic Sites: An Experimental and Theoretical Study. *Chem. Commun.* **2015**, *51*, 13918−13921.
(12) Yan, Y.; Juríček, M.; Coudert, F. X.; Vermeulen, N. A.; Grunder, S.; Dailly, A.; Lewis, W.; Blake, A. J.; Stoddart, J. F.; Schröder, M. Non-Interpenetrated Metal-Organic Frameworks Based on Copper(II) Paddlewheel and Oligoparaxylene-Isophthalate Linkers: Synthesis, Structure, and Gas Adsorption. *J. Am. Chem. Soc.* **2016**, *138*, 3371−3381.
(13) Bajpai, A.; O'Nolan, D.; Madden, D. G.; Chen, K.-J.; Pham, T.; Kumar, A.; Lusi, M.; Perry, J. J.; Space, B.; Zaworotko, M. J. The Effect of Centred Versus Offset Interpenetration on $C_2H_2$ Sorption in Hybrid Ultramicroporous Materials. *Chem. Commun.* **2017**, *53*, 11592−11595.
(14) O'Nolan, D.; Madden, D. G.; Kumar, A.; Chen, K.-J.; Pham, T.; Forrest, K. A.; Patyk-Kazmierczak, E.; Yang, Q.-Y.; Murray, C. A.; Tang, C. C.; Space, B.; Zaworotko, M. J. Impact of Partial Interpenetration in a Hybrid Ultramicroporous Material on $C_2H_2$/$C_2H_4$ Separation Performance. *Chem. Commun.* **2018**, *54*, 3488−3491.
(15) Zhao, Y. C.; Wang, J. W.; Bao, Z. B.; Xing, H. B.; Zhang, Z. G.; Su, B. G.; Yang, Q. W.; Yang, Y. W.; Ren, Q. L. Adsorption Separation of Acetylene and Ethylene in a Highly Thermostable Microporous Metal-Organic Framework. *Sep. Purif. Technol.* **2018**, *195*, 238−243.
(16) Fan, W.; Wang, X.; Zhang, X.; Liu, X.; Wang, Y.; Kang, Z.; Dai, F.; Xu, B.; Wang, R.; Sun, D. Fine-Tuning the Pore Environment of the Microporous Cu-MOF for High Propylene Storage and Efficient Separation of Light Hydrocarbons. *ACS Cent. Sci.* **2019**, *5*, 1261−1268.
(17) Wang, X.; Zhang, X. R.; Zhang, K.; Wang, X. K.; Wang, Y. T.; Fan, W. D.; Dai, F. N. Amino-Functionalized Cu-MOF for Efficient Purification of Methane from Light Hydrocarbons and Excellent Catalytic Performance. *Inorg. Chem. Front.* **2019**, *6*, 1152−1157.
(18) Bao, Z. B.; Chang, G. G.; Xing, H. B.; Krishna, R.; Ren, Q. L.; Chen, B. Potential of Microporous Metal-Organic Frameworks for Separation of Hydrocarbon Mixtures. *Energy Environ. Sci.* **2016**, *9*, 3612−3641.
(19) Herm, Z. R.; Bloch, E. D.; Long, J. R. Hydrocarbon Separations in Metal-Organic Frameworks. *Chem. Mater.* **2014**, *26*, 323−338.
(20) Geier, S. J.; Mason, J. A.; Bloch, E. D.; Queen, W. L.; Hudson, M. R.; Brown, C. M.; Long, J. R. Selective Adsorption of Ethylene over Ethane and Propylene over Propane in the Metal−Organic Frameworks $M_2$(dobdc) (M = Mg, Mn, Fe, Co, Ni, Zn). *Chem. Sci.* **2013**, *4*, 2054−2061.
(21) Cui, X.; Chen, K.; Xing, H. B.; Yang, Q.; Krishna, R.; Bao, Z. B.; Wu, H.; Zhou, W.; Dong, X.; Han, Y.; Li, B.; Ren, Q.; Zaworotko, M. J.; Chen, B. Pore Chemistry and Size Control in Hybrid Porous Materials for Acetylene Capture from Ethylene. *Science* **2016**, *353*, 141−144.
(22) Li, L.; Lin, R.-B.; Krishna, R.; Li, H.; Xiang, S.; Wu, H.; Li, J.; Zhou, W.; Chen, B. Ethane/Ethylene Separation in a Metal-Organic Framework with Iron-Peroxo Sites. *Science* **2018**, *362*, 443−446.
(23) Liao, P.-Q.; Zhang, W.-X.; Zhang, J.-P.; Chen, X.-M. Efficient Purification of Ethene by an Ethane-Trapping Metal-Organic Framework. *Nat. Commun.* **2015**, *6*, No. 8697.
(24) Liang, W. W.; Xu, F.; Zhou, X.; Xiao, J.; Xia, Q. B.; Li, Y. W.; Li, Z. Ethane Selective Adsorbent Ni(bdc)$(ted)_{0.5}$ with High Uptake and its Significance in Adsorption Separation of Ethane and Ethylene. *Chem. Eng. Sci.* **2016**, *148*, 275−281.
(25) Qazvini, O. T.; Babarao, R.; Shi, Z.-L.; Zhang, Y.-B.; Telfer, S. G. A Robust Ethane-Trapping Metal-Organic Framework with a High Capacity for Ethylene Purification. *J. Am. Chem. Soc.* **2019**, *141*, 5014−5020.
(26) Zeng, H.; Xie, X.-J.; Xie, M.; Huang, Y.-L.; Luo, D.; Wang, T.; Zhao, Y.; Lu, W.; Li, D. Cage-Interconnected Metal-Organic Framework with Tailored Apertures for Efficient $C_2H_6/C_2H_4$ Separation under Humid Conditions. *J. Am. Chem. Soc.* **2019**, *141*, 20390−20396.
(27) Dolomanov, O. V.; Bourhis, L. J.; Gildea, R. J.; Howard, J. A. K.; Puschmann, H. OLEX2: A Complete Structure Solution, Refinement and Analysis Program. *J. Appl. Crystallogr.* **2009**, *42*, 339−341.
(28) Michaels, H. High Pressure Synchrotron Radiation Crystallography, from Organic Conductors to Chemistry in the Lower Mantle. *Acta Crystallogr., Sect. A: Found. Adv.* **2015**, *71*, 3−8.
(29) Sazanov, L. A. Structure and Mechanism of Respiratory Complex I, A Giant Molecular Proton Pump. *Acta Crystallogr., Sect. C: Struct. Chem.* **2015**, *71*, s3.
(30) Chen, Y. W.; Qiao, Z. W.; Wu, H. X.; Lv, D. F.; Shi, R. F.; Xia, Q. B.; Zhou, J.; Li, Z. An Ethane-Trapping MOF PCN-250 for Highly Selective Adsorption of Ethane over Ethylene. *Chem. Eng. Sci.* **2018**, *175*, 110−117.
(31) Pires, J.; Pinto, M. L.; Saini, V. K. Ethane Selective IRMOF-8 and its Significance in Ethane-Ethylene Separation by Adsorption. *ACS Appl. Mater. Interfaces* **2014**, *6*, 12093−12099.
(32) Lv, D.; Shi, R.; Chen, Y.; Wu, Y.; Wu, H.; Xi, H.; Xia, Q.; Li, Z. Selective Adsorption of Ethane over Ethylene in PCN-245: Impacts of Interpenetrated Adsorbent. *ACS Appl. Mater. Interfaces* **2018**, *10*, 8366−8373.
(33) Zhou, D.-D.; He, C.-T.; Liao, P.-Q.; Xue, W.; Zhang, W.-X.; Zhou, H.-L.; Zhang, J.-P.; Chen, X.-M. A Flexible Porous Cu(II) Bis-Imidazolate Framework with Ultrahigh Concentration of Active Sites for Efficient and Recyclable $CO_2$ Capture. *Chem. Commun.* **2013**, *49*, 11728−11730.
(34) Wu, Y.; Chen, H. Y.; Liu, D. F.; Qian, Y.; Xi, H. X. Adsorption and Separation of Ethane/Ethylene on ZIFs with Various Topologies: Combining GCMC Simulation with the Ideal Adsorbed Solution Theory (IAST). *Chem. Eng. Sci.* **2015**, *124*, 144−153.
(35) Yuan, W. H.; Zhang, X. T.; Li, L. Synthesis of Zeolitic Imidazolate Framework-69 for Adsorption Separation of Ethane and Ethylene. *J. Solid State Chem.* **2017**, *251*, 198−203.
(36) Cai, J. F.; Yu, J. C.; Xu, H.; He, Y. B.; Duan, X.; Cui, Y. J.; Wu, C. D.; Chen, B.; Qian, G. D. A Doubly Interpenetrated Metal-Organic Framework with Open Metal Sites and Suitable Pore Sizes for Highly


https://dx.doi.org/10.1021/acsami.9b22410
*ACS Appl. Mater. Interfaces* 2020, 12, 6105−6111

Selective Separation of Small Hydrocarbons at Room Temperature. *Cryst. Growth Des.* **2013**, *13*, 2094−2097.
(37) Gücüyener, C.; van den Bergh, J.; Gascon, J.; Kapteijn, F. Ethane/Ethene Separation Turned on Its Head: Selective Ethane Adsorption on the Metal-Organic Framework ZIF-7 Through a Gate-Opening Mechanism. *J. Am. Chem. Soc.* **2010**, *132*, 17704−17706.
(38) He, Y.; Zhang, Z.; Xiang, S.; Fronczek, F. R.; Krishna, R.; Chen, B. A Microporous Metal-Organic Framework for Highly Selective Separation of Acetylene, Ethylene, and Ethane from Methane at Room Temperature. *Chem. - Eur. J.* **2012**, *18*, 613−619.
(39) Chen, Y. W.; Wu, H. X.; Lv, D. F.; Shi, R. F.; Chen, Y.; Xia, Q. B.; Li, Z. Highly Adsorptive Separation of Ethane/Ethylene by an Ethane-Selective MOF MIL-142A. *Ind. Eng. Chem. Res.* **2018**, *57*, 4063−4069.
(40) He, Y.; Zhang, Z.; Xiang, S.; Fronczek, F. R.; Krishna, R.; Chen, B. A Robust Doubly Interpenetrated Metal-Organic Framework Constructed from a Novel Aromatic Tricarboxylate for Highly Selective Separation of Small Hydrocarbons. *Chem. Commun.* **2012**, *48*, 6493−6495.
(41) Lin, R.-B.; Wu, H.; Li, L.; Tang, X.-L.; Li, Z.; Gao, J.; Cui, H.; Zhou, W.; Chen, B. Boosting Ethane/Ethylene Separation within Isoreticular Ultramicroporous Metal-Organic Frameworks. *J. Am. Chem. Soc.* **2018**, *140*, 12940−12946.



https://dx.doi.org/10.1021/acsami.9b22410
*ACS Appl. Mater. Interfaces* 2020, 12, 6105−6111

# Supporting Information

## A microporous metal-organic framework with a completely reversed adsorption relationship for $C_2$ hydrocarbons at room temperature

*Fang-Zhou Sun,[a] Shan-Qing Yang,[a] Rajamani Krishna,[c] Ying-Hui Zhang,[a,b] Yu-Pei Xia[a] and Tong-Liang Hu*[a,b]*

[a]School of Materials Science and Engineering, Nankai University, Tianjin 300350, China. E-mail: tlhu@nankai.edu.cn.

[b]Tianjin Key Lab for Rare Earth Materials and Applications, and Key Laboratory of Advanced Energy Material Chemistry (Ministry of Education), Nankai University, Tianjin 300350, China.

[c]Van 't Hoff Institute for Molecular Sciences, University of Amsterdam, Science Park 904, 1098 XH Amsterdam, The Netherlands

## Grand Canonical Monte Carlo (GCMC) Simulations

The Grand Canonical Monte Carlo (GCMC) simulations were performed for $C_2H_6$, $C_2H_4$ and $C_2H_2$ adsorption on **NUM-7a**. The framework of **NUM-7a** and gas molecules were both treated as rigid bodies. The beneficial adsorption sites were simulated by the fixed loading task and Metropolis method at 298 K and 1 bar. The loading steps, equilibration steps and the production steps were all set to $2.0 \times 10^7$. The saturation/maximum uptakes were modeled at 298 K using the fixed pressure task with $1.0 \times 10^5$ equilibration steps, followed by $2.0 \times 10^7$ production steps for calculating the ensemble averages. The gas–framework interaction and the gas–gas interaction were described by the standard universal force field (UFF). The atomic partial charges of the framework were used for Qeq method, the guest gas molecules were optimized using the DMol3 method and adopted the B3LYP fitted charge. The cut-off radius used for the Lennard–Jones interactions is 18.5 Å.[1,2]

## Fitting of pure component isotherms

The isotherm data for $C_2H_6$, $C_2H_4$, $CO_2$ and $CH_4$ in **NUM-7a**, measured at 298 K, were fitted with the Dual-site Langmuir model.

$$q = q_{A,sat}\frac{b_A p}{1+b_A p} + q_{B,sat}\frac{b_B p}{1+b_B p}$$

## IAST calculations of adsorption selectivities, and uptake capacities

In order to determine the $C_2H_6/C_2H_4$, $C_2H_2/CO_2$ and $CO_2/CH_4$ separation potential of **NUM-7a**, IAST calculations of 50/50 and 10/90 mixture adsorption at 298 K were performed by

$$S_{ads} = \frac{q_1/q_2}{p_1/p_2}$$

## Breakthrough simulations

The performance of industrial fixed bed adsorber is dictated by a combination of adsorption selectivity and uptake capacity. Transient breakthrough simulations were carried out for 50/50 and 10/90 $C_2H_6/C_2H_4$ mixtures in **NUM-7a** operating at a total pressure of 100 kPa and 298 K, using the methodology described in earlier publications.[3-6] For the breakthrough simulations, the following parameter values were used: length of packed bed, $L$ = 0.3 m; voidage of packed bed, $\varepsilon$ = 0.4; superficial gas velocity at inlet, $u$ = 0.04 m $s^{-1}$.

## Notation

| | |
|---|---|
| $b$ | Langmuir-Freundlich constant, $Pa^{-\nu}$ |
| $q$ | component molar loading of species $i$, mol $kg^{-1}$ |
| $q_{sat}$ | saturation loading, mol $kg^{-1}$ |
| $L$ | length of packed bed adsorber, m |
| $t$ | time, s |
| $T$ | absolute temperature, K |
| $u$ | superficial gas velocity in packed bed, m $s^{-1}$ |

## Greek letters

| | |
|---|---|
| $\varepsilon$ | voidage of packed bed, dimensionless |
| $\nu$ | Freundlich exponent, dimensionless |
| $\tau$ | time, dimensionless |

**Table S1.** Crystal data and structure refinement parameters for **NUM-7**.

| | **NUM-7** |
|---|---|
| Formula | $C_{38}H_{35}Mn_2N_3O_{11}$ |
| *M*r (g mol$^{-1}$) | 819.57 |
| Space group | $P2_1/c$ |
| Crystal system | Monoclinic |
| *a* (Å) | 11.6212(1) |
| *b* (Å) | 13.0997(2) |
| *c* (Å) | 25.0298(3) |
| $\beta$(°) | 97.156(1) |
| *V* (Å$^3$) | 3780.71(8) |
| *Z* | 4 |
| *F*(000) | 1688.0 |
| *Dc* (gcm$^{-3}$) | 1.440 |
| $\mu$ (mm$^{-1}$) | 5.978 |
| GOF on $F^2$ | 1.055 |
| $R_1$, $wR_2$ [$I>2\sigma(I)$][a] | 0.0461, 0.1305 |
| $R_1$, $wR_2$ [all data][b] | 0.0503, 0.1305 |

[a] $R_1 = \sum ||F_o| - |F_c|| / \sum |F_o|$. [b] $wR_2 = \{\sum[w(F_o^2 - F_c^2)^2] / \sum w(F_o^2)^2\}^{1/2}$

**Table S2.** Langmuir-Freundlich parameter fits for $C_2H_4$ and $C_2H_6$ in **NUM-7a** at 298 K.

| | $q_{sat}$ mol kg$^{-1}$ | $b$ Pa$^{-v}$ | dimensionless |
|---|---|---|---|
| $C_2H_4$ | 3.1 | 8.07425E-05 | 0.96 |
| $C_2H_6$ | 3.1 | 6.25788E-05 | 1.05 |

**Table S3.** IAST selectivity comparison of $C_2H_6$-selectivity MOFs.

| | **298 K $C_2H_6$ adsorbed amount ($cm^3\ g^{-1}$) (1 bar)** | **298 K $C_2H_4$ adsorbed amount ($cm^3\ g^{-1}$) (1 bar)** | **Selectivity (50:50) (1 bar)** | **Ref.** |
|---|---|---|---|---|
| **$Fe(O_2)$dobdc** | 76 | 57 | 4.25 | 7 |
| **$Cu(Qc)_2$** | 41 | 17 | 3.4 | 8 |
| **MUF-15 (293 K)** | 105 | 93 | 1.95 | 9 |
| **PCN-250** | 116 | 94 | 1.9 | 10 |
| **PCN-245** | 73 | 54 | 1.8 | 11 |
| **NUM-7a** | 68 | 60 | **1.76** | **This work** |
| **ZJU-30** | 47 | 44 | ＜1.7 | 12 |
| **ZIF-69** | 49 | 39 | 1.66 | 13 |
| **$Ni(bdc)(ted)_{0.5}$** | 112 | 76 | 1.6 | 14 |
| **MIL-142-A** | 85 | 65 | 1.5 | 15 |
| **ZIF-7** | 41 | 40 | 1.5 | 16 |
| **UTSA-33** | 83 | 76 | 1. 4 | 17 |
| **UTSA-35** | 54 | 48 | 1.4 | 18 |
| **$Cu(ina)_2$** | 44 | 42 | 1.34 | 8 |

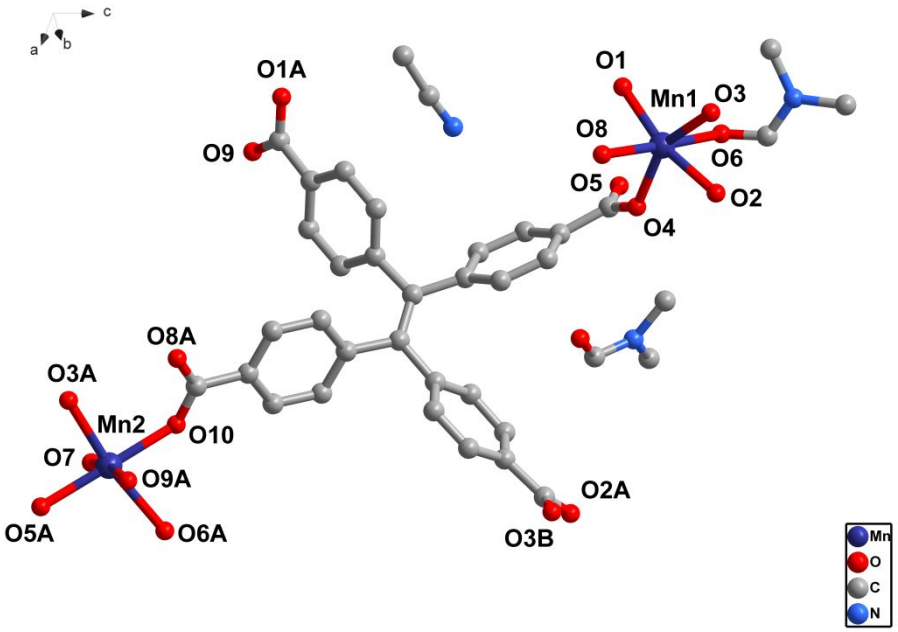


**Figure S1.** The asymmetric unit for **NUM-7** (Hydrogen atoms were omitted.).

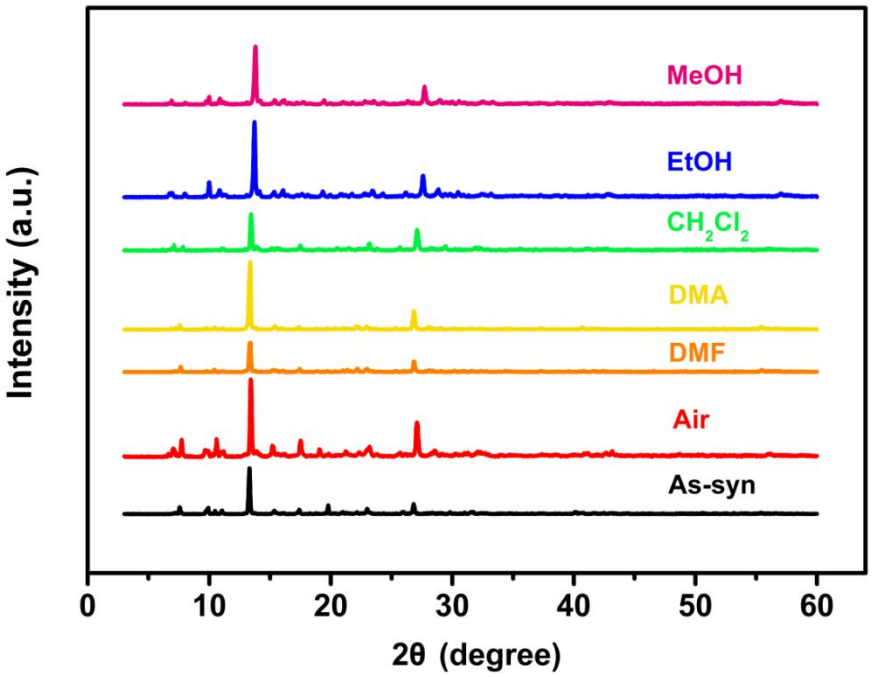


**Figure S2.** PXRD patterns for **NUM-7** in some solvents for 1 day, showing the structural integrity.

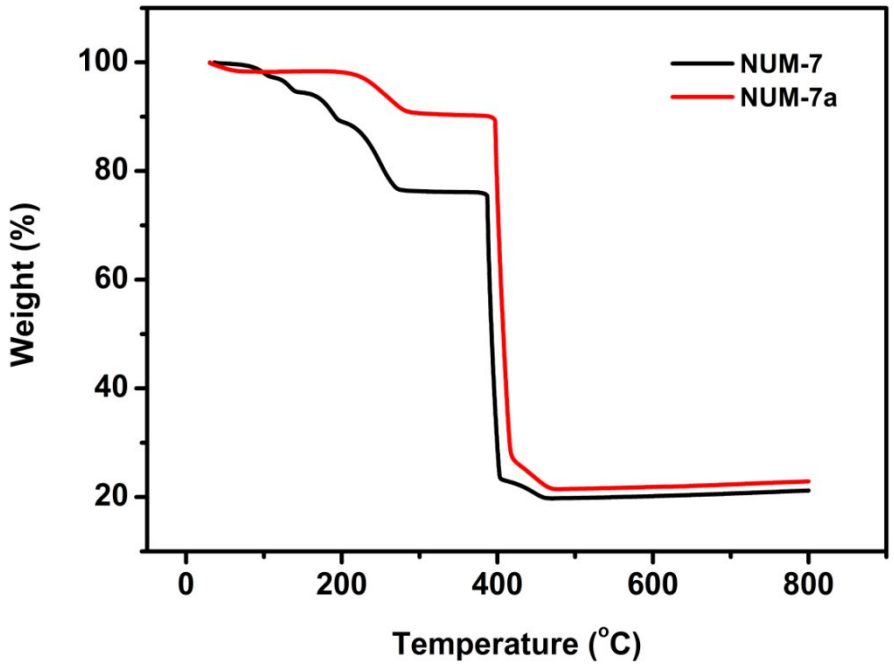


**Figure S3.** TGA curves for **NUM-7** and **NUM-7a** under air atmosphere.

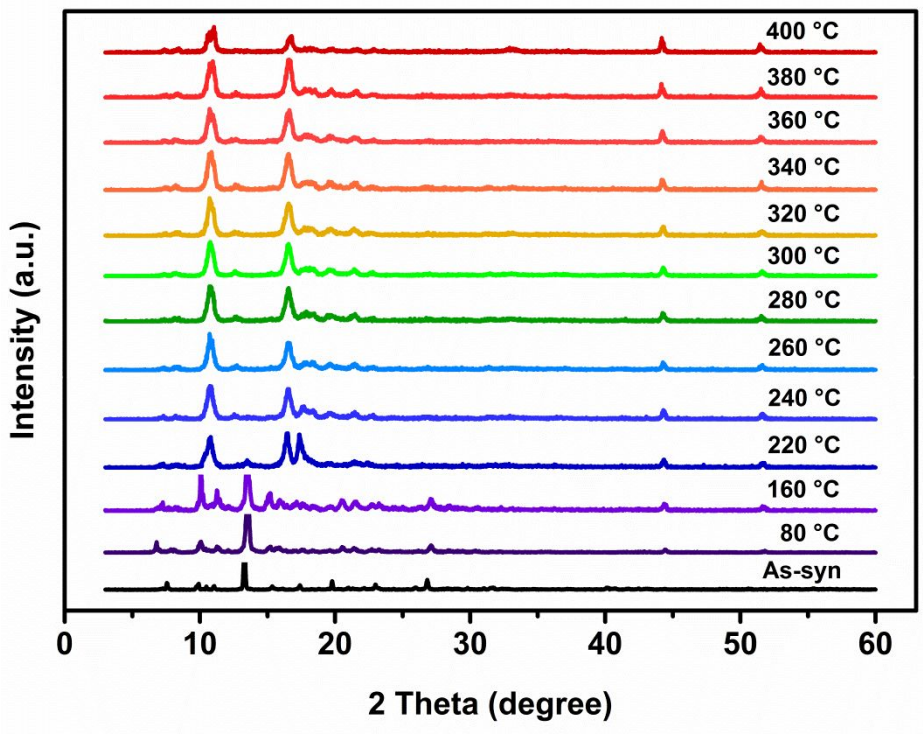


**Figure S4.** VT-PXRD patterns of **NUM-7** under air atmosphere.

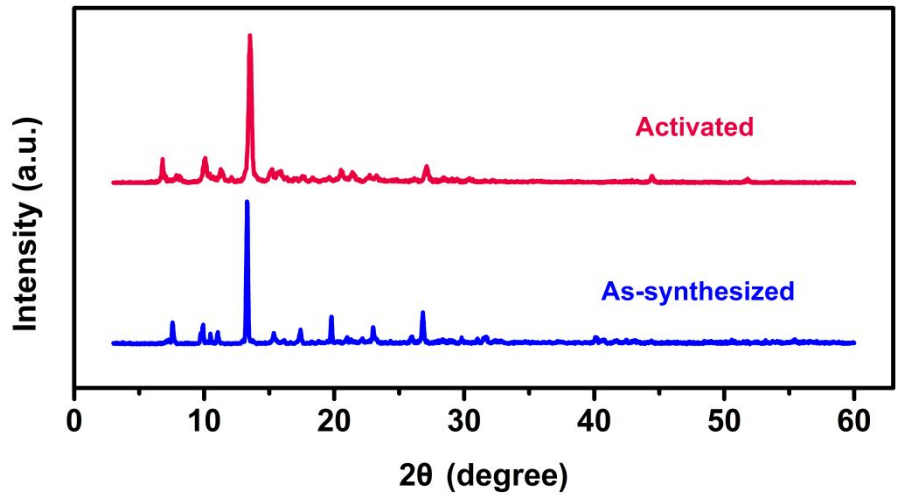


**Figure S5.** PXRD patterns of **NUM-7** showing that the structure still remains unchanged after activation at 150 °C under vacuum.

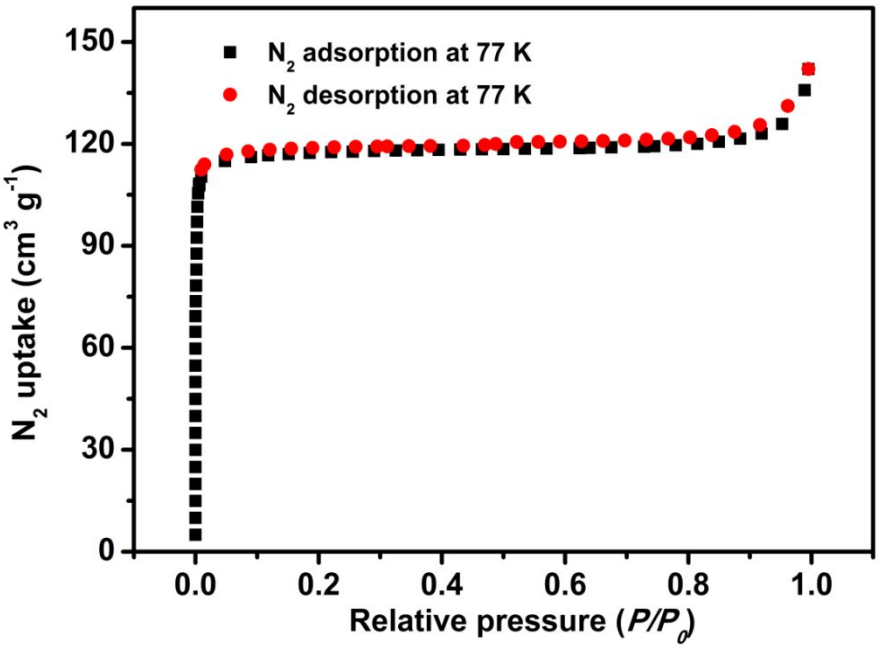


**Figure S6.** Volumetric $N_2$ adsorption isotherm for **NUM-7a** at 77 K.

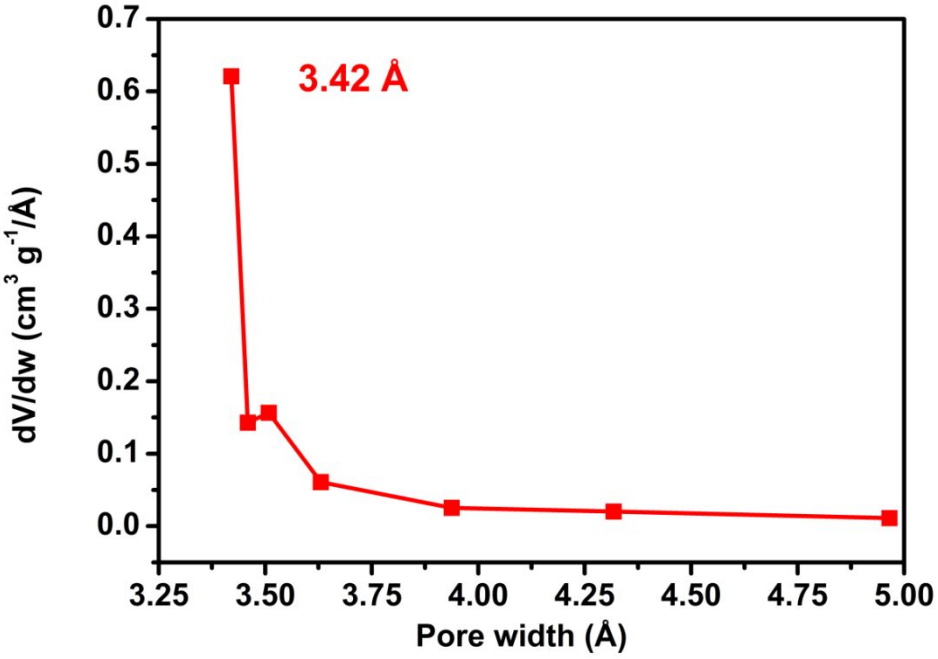


**Figure S7.** The pore size distribution for **NUM-7a**.

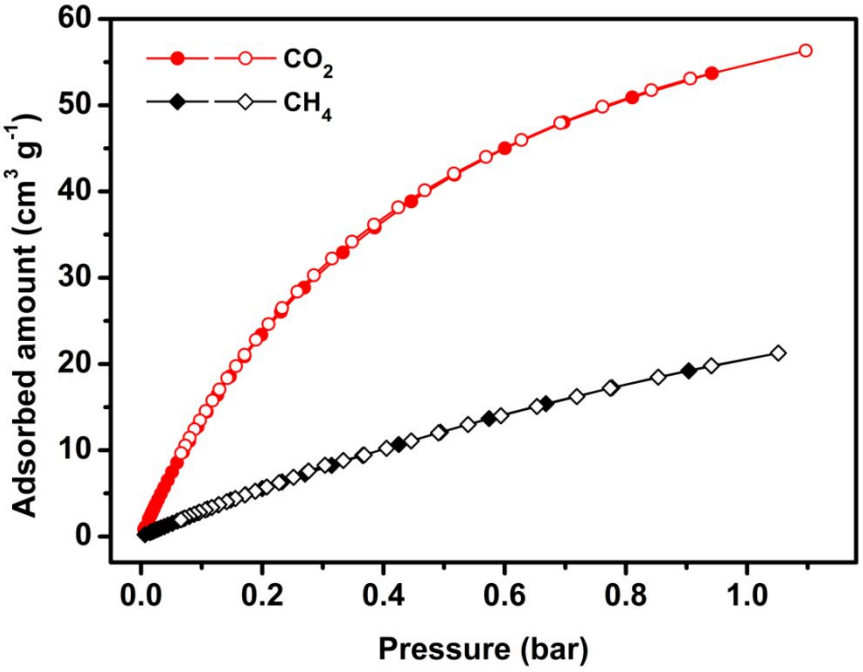


**Figure S8.** $CO_2$, $CH_4$ adsorption isotherms for **NUM-7a** at 273 K.

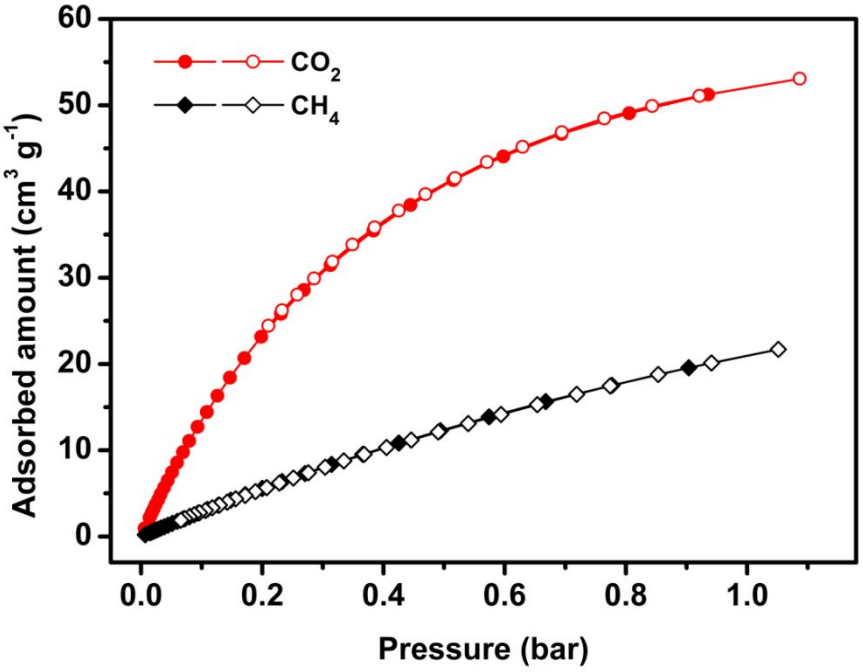


**Figure S9.** $CO_2$, $CH_4$ adsorption isotherms for **NUM-7a** at 298 K.

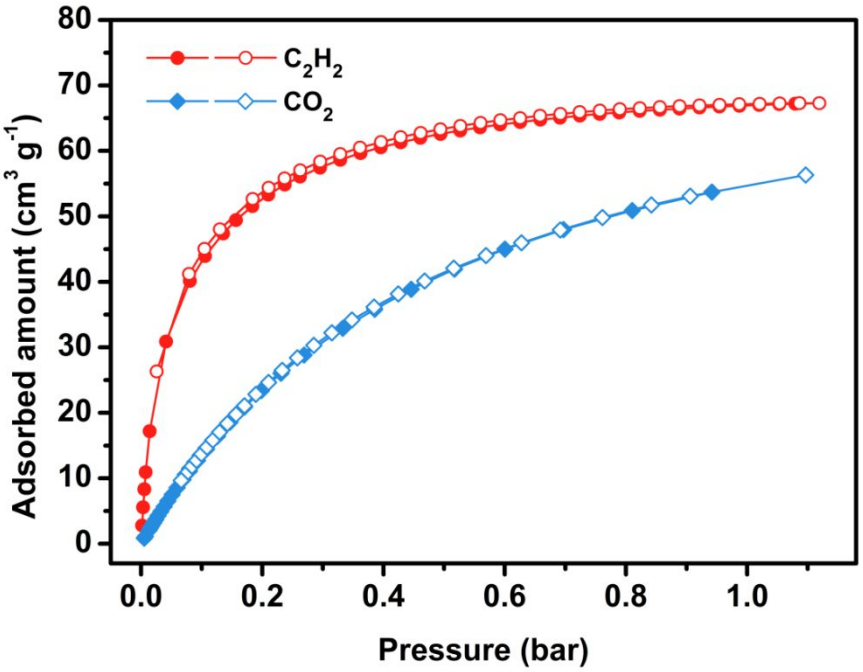


**Figure S10.** $C_2H_2$, $CO_2$ adsorption isotherms for **NUM-7a** at 273 K.

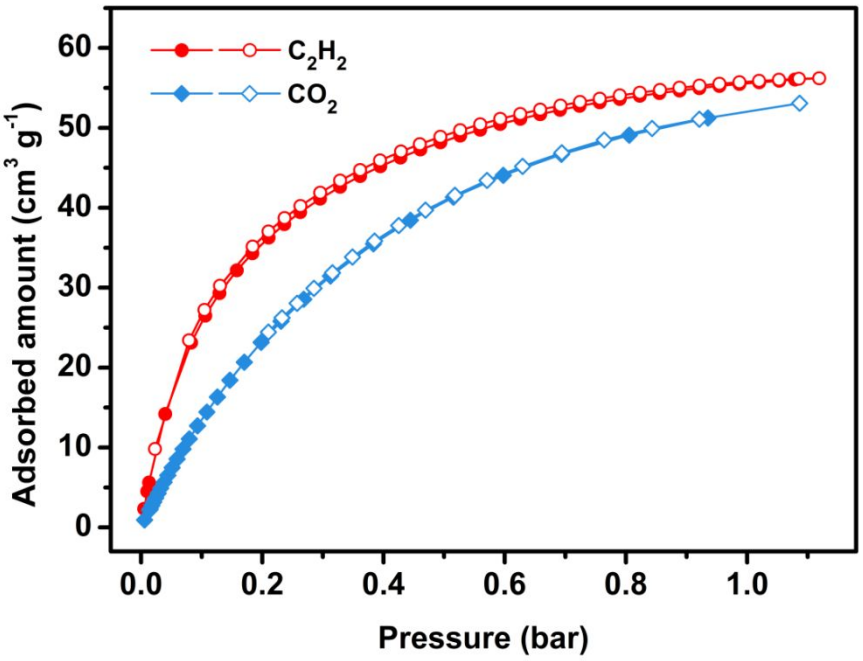


**Figure S11.** $C_2H_2$, $CO_2$ adsorption isotherms for **NUM-7a** at 298 K.

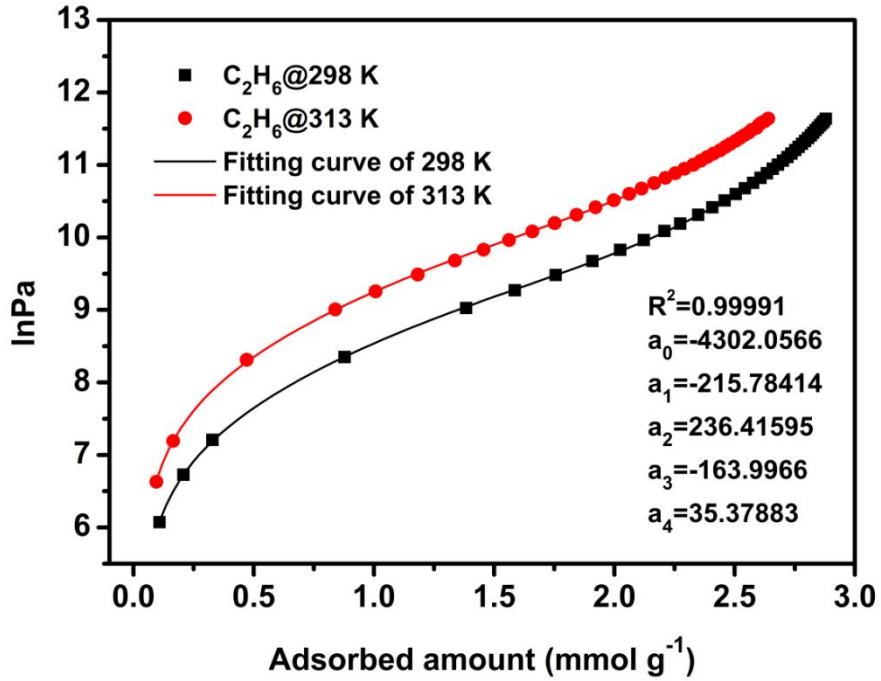


**Figure S12.** The details of virial equation (solid lines) fitting to the experimental $C_2H_6$ adsorption data (symbols) for **NUM-7a**.

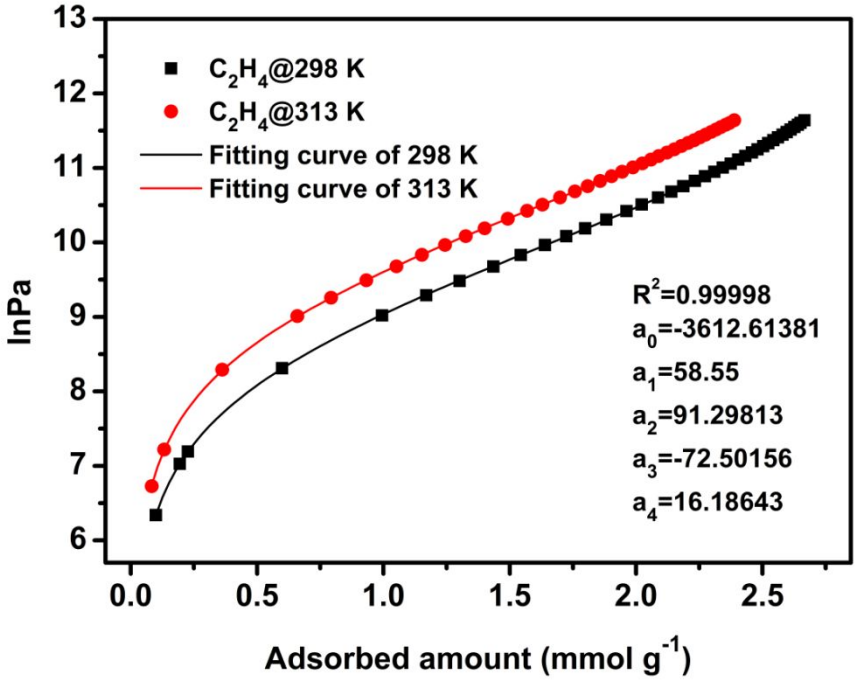


**Figure S13.** The details of virial equation (solid lines) fitting to the experimental $C_2H_4$ adsorption data (symbols) for **NUM-7a**.

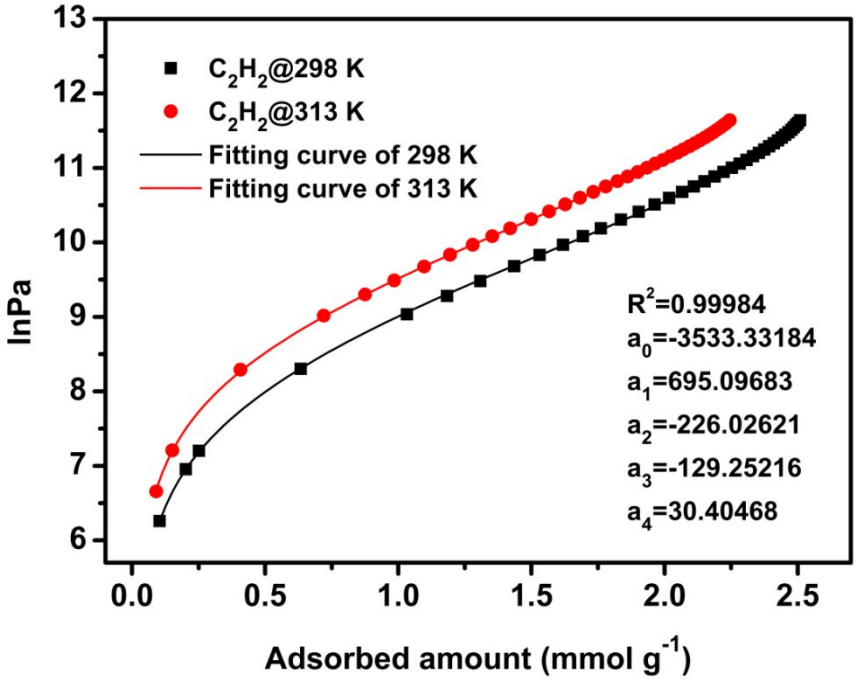


**Figure S14.** The details of virial equation (solid lines) fitting to the experimental $C_2H_2$ adsorption data (symbols) for **NUM-7a**.

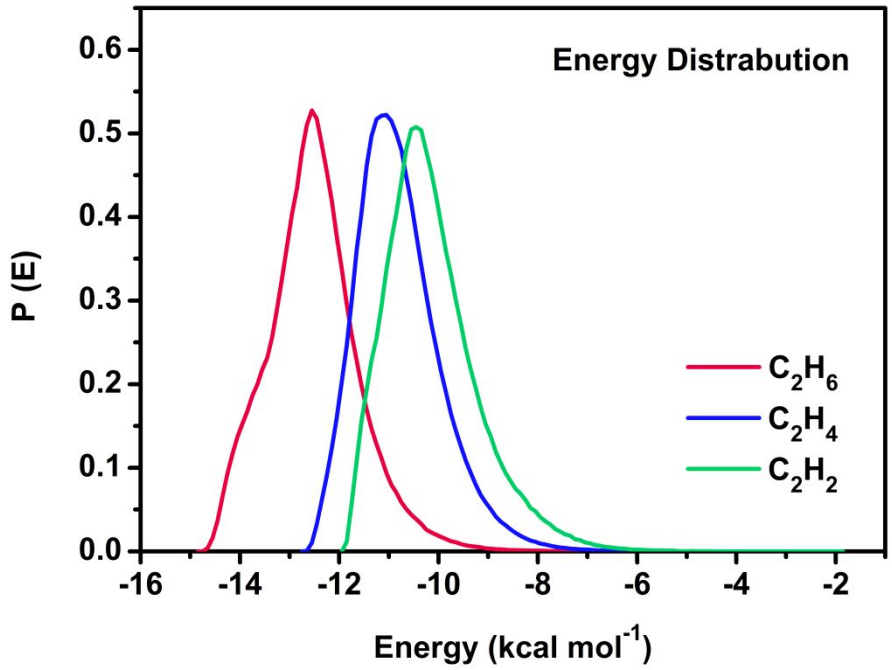


**Figure S15.** Isosteric heats of $C_2H_6$ $C_2H_4$ and $C_2H_2$.

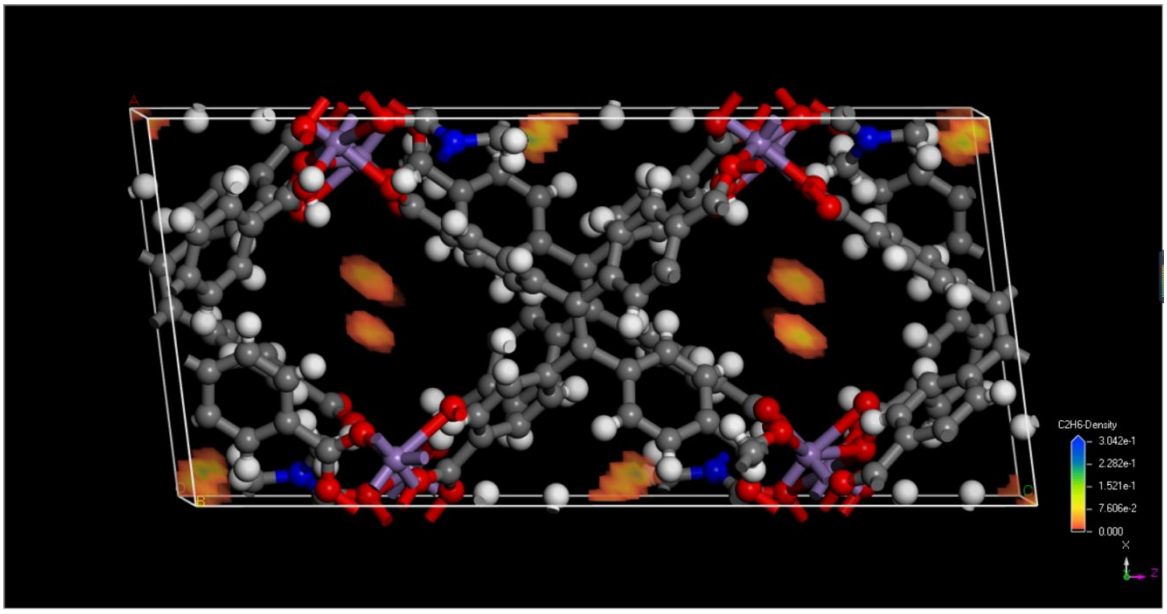


**Figure S16.** Density distribution of $C_2H_6$ in **NUM-7a**.

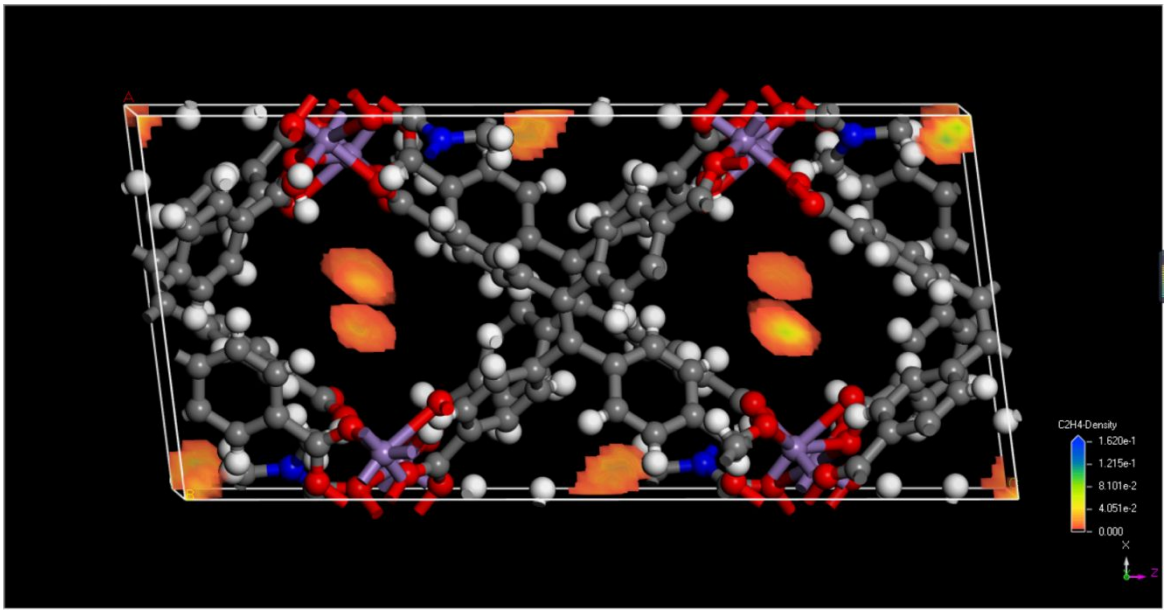


**Figure S17.** Density distribution of $C_2H_4$ in **NUM-7a**.

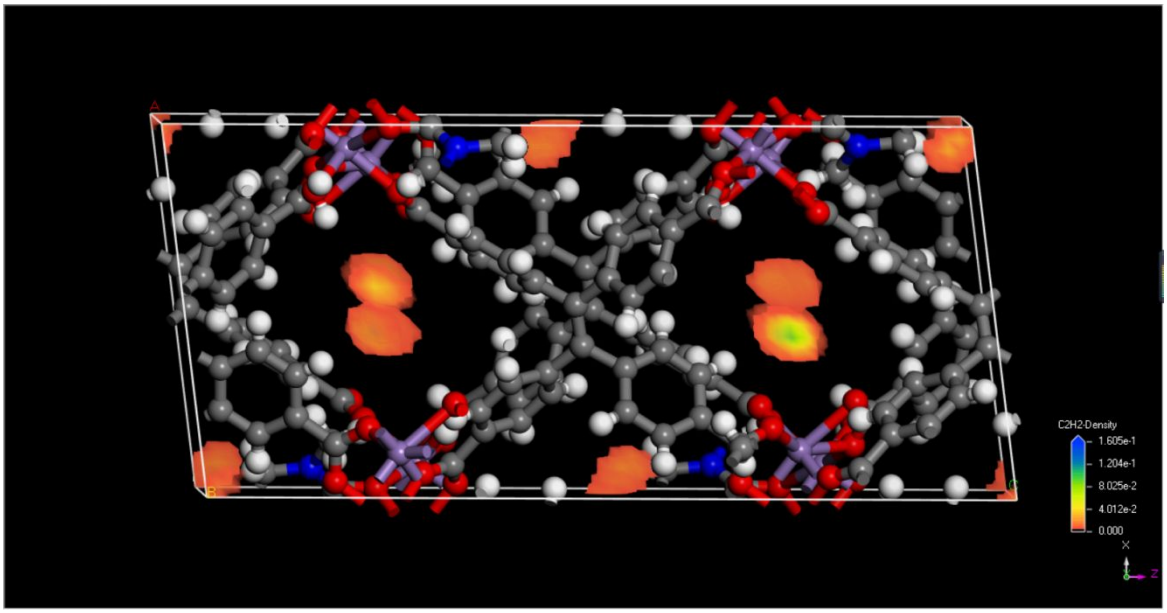


**Figure S18.** Density distribution of $C_2H_2$ in **NUM-7a**.

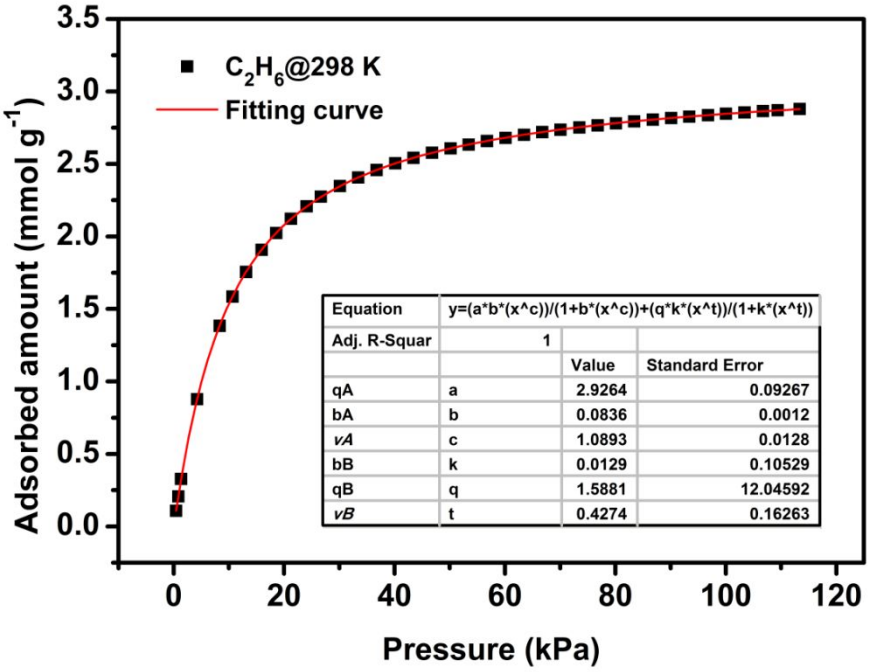


**Figure S19.** $C_2H_6$ adsorption isotherm for **NUM-7a** (symbols) at 298 K and the virial equation fit (line) by Langmuir-Freundlich (L-F) model.

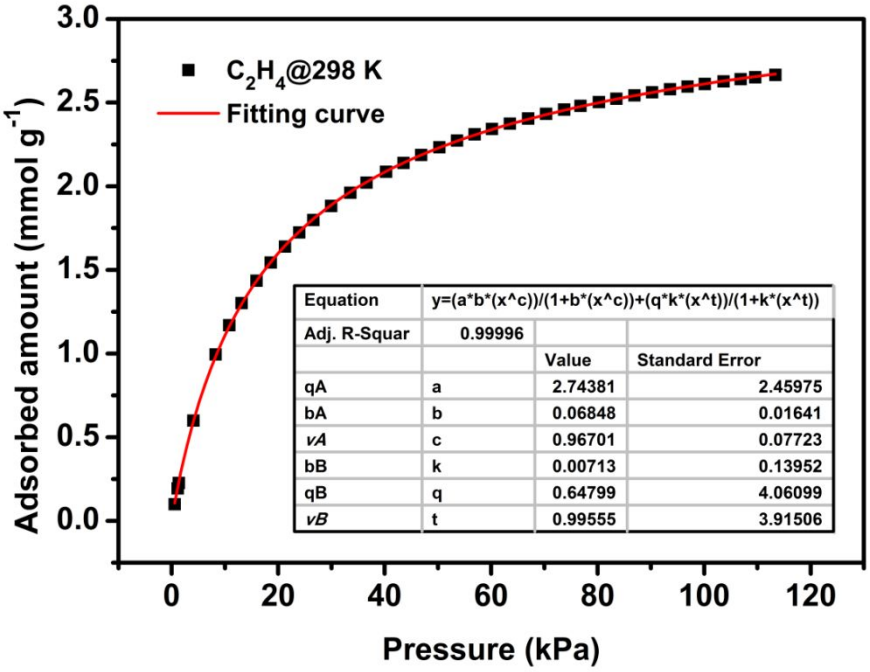


**Figure S20.** $C_2H_4$ adsorption isotherm for **NUM-7a** (symbols) at 298 K and the virial equation fit (line) by Langmuir-Freundlich (L-F) model.

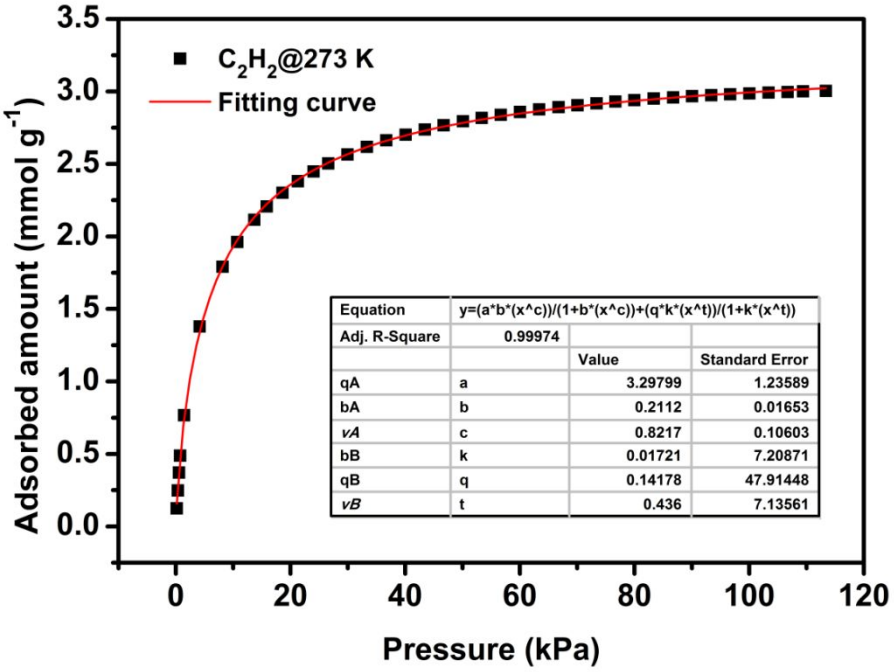


**Figure S21.** $C_2H_2$ adsorption isotherm for **NUM-7a** (symbols) at 273 K and the virial equation fit (line) by Langmuir-Freundlich (L-F) model.

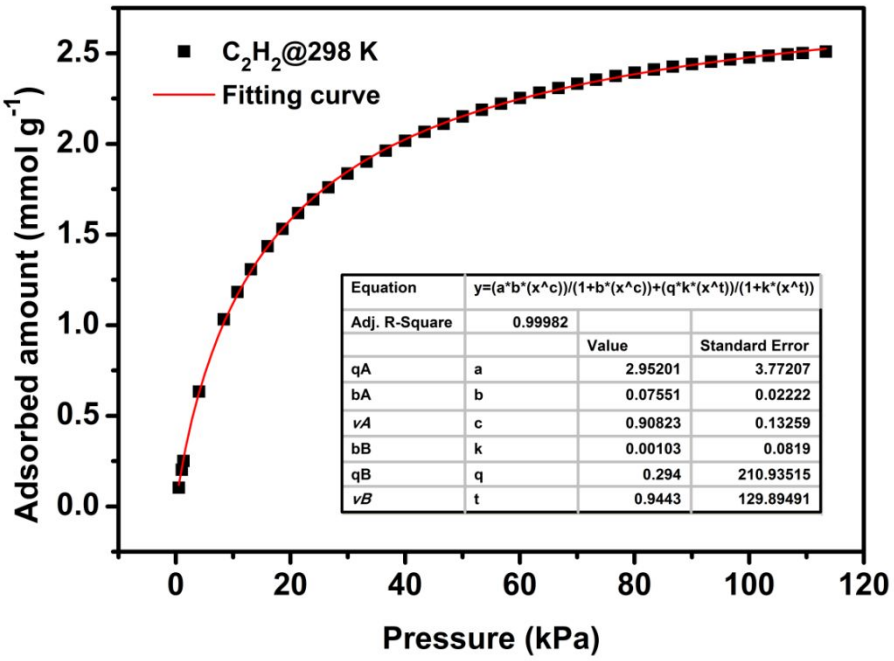


**Figure S22.** $C_2H_2$ adsorption isotherm for **NUM-7a** (symbols) at 298 K and the virial equation fit (line) by Langmuir-Freundlich (L-F) model.

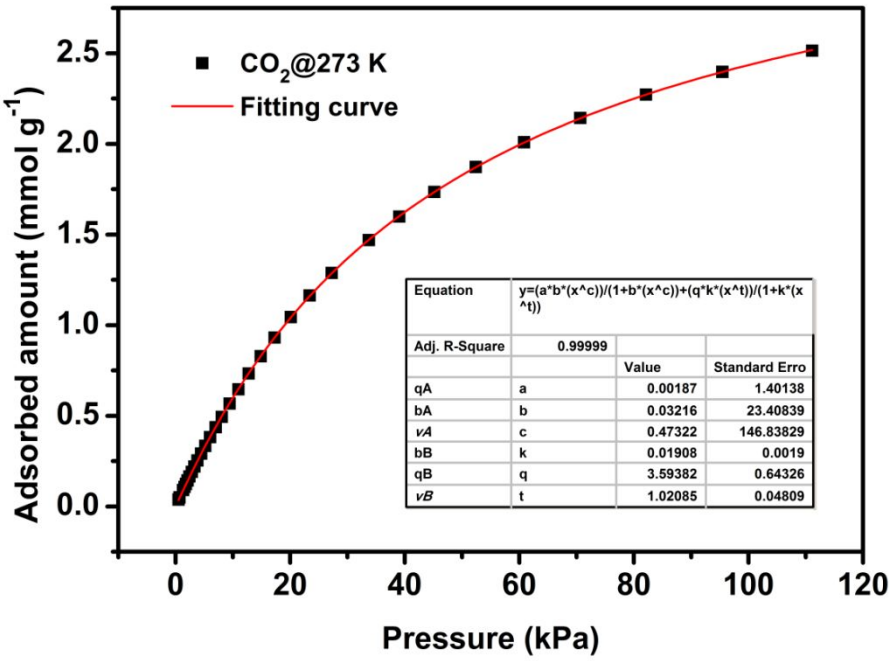


**Figure S23.** $CO_2$ adsorption isotherm for **NUM-7a** (symbols) at 273 K and the virial equation fit (line) by Langmuir-Freundlich (L-F) model.

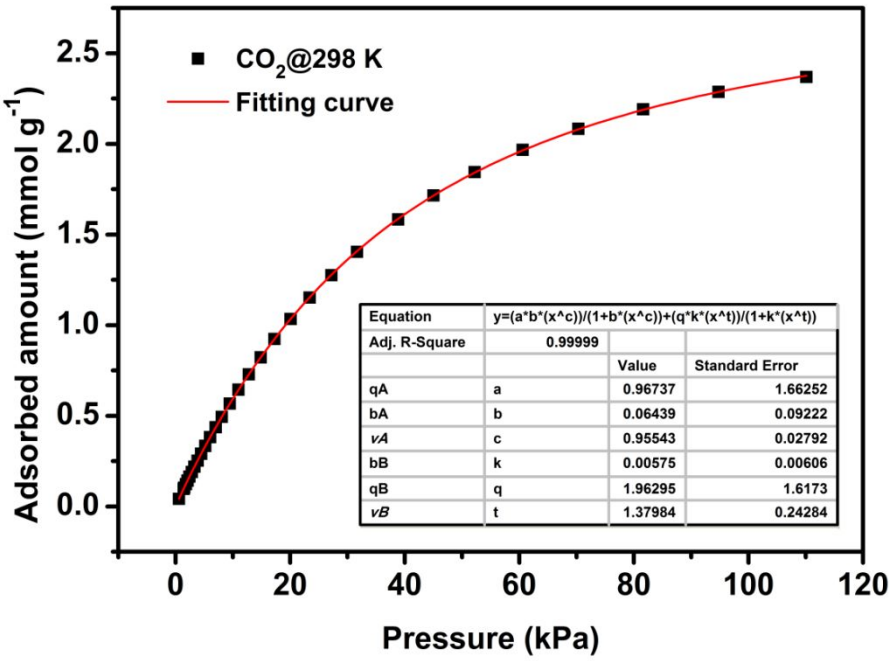


**Figure S24.** $CO_2$ adsorption isotherm for **NUM-7a** (symbols) at 298 K and the virial equation fit (line) by Langmuir-Freundlich (L-F) model.

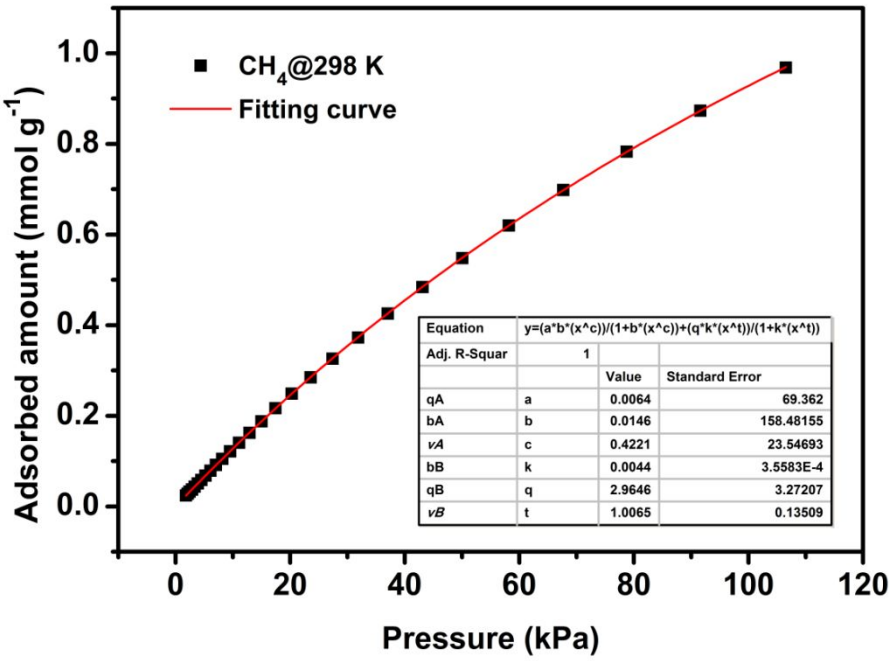


**Figure S25.** $CH_4$ adsorption isotherm for **NUM-7a** (symbols) at 298 K and the virial equation fit (line) by Langmuir-Freundlich (L-F) model.

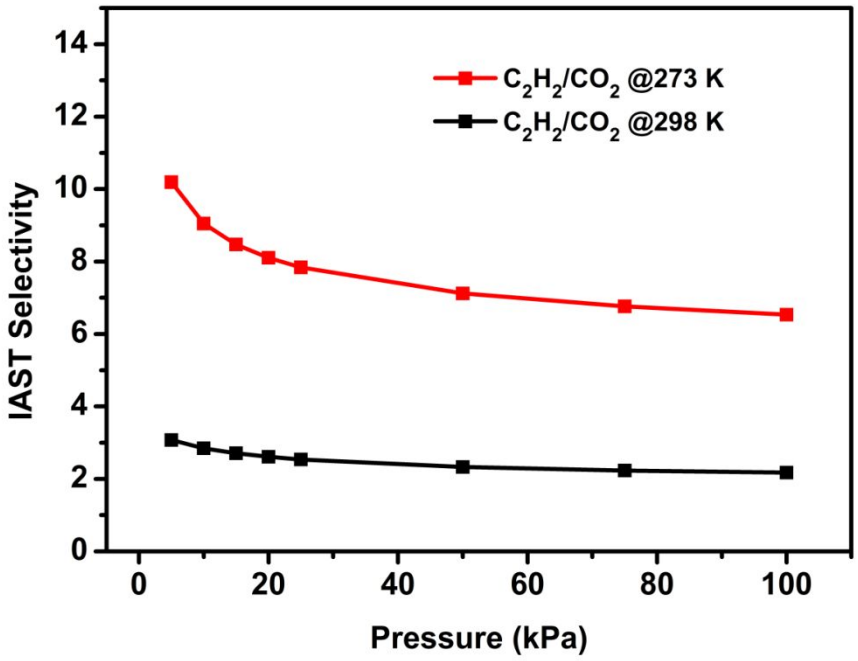


**Figure S26.** IAST selectivity of $C_2H_2/CO_2$ (50/50) for **NUM-7a**.

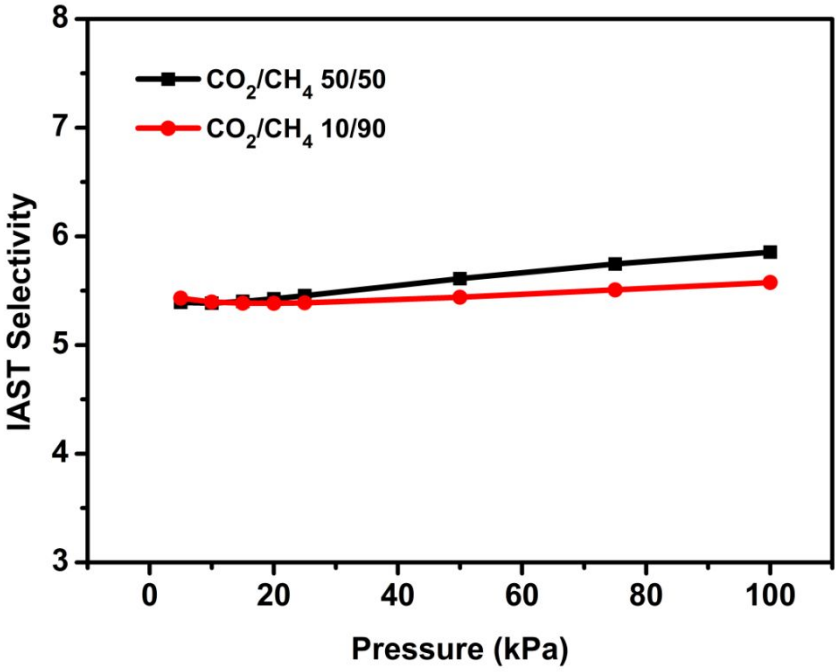


**Figure S27.** IAST selectivity of $CO_2/CH_4$ (50/50 and 10/90) for **NUM-7a** at 298 K.

## References


1. Zhou, D. D.; He, C. T.; Liao, P. Q.; Xue, W.; Zhang, W. X.; Zhou, H. L.; Zhang, J. P.; Chen, X. M. A Flexible Porous Cu(II) Bis-Imidazolate Framework with Ultrahigh Concentration of Active Sites for Efficient and Recyclable $CO_2$ Capture. *Chem. Commun.* **2013**, *49*, 11728-11730.
2. Wu, Y.; Chen, H. Y.; Liu, D. F.; Qian, Y.; Xi, H. X. Adsorption and Separation of Ethane/Ethylene on ZIFs with Various Topologies: Combining GCMC Simulation with the Ideal Adsorbed Solution Theory (IAST). *Chem. Eng. Sci.* **2015**, *124*, 144-153.
3. Krishna, R. The Maxwell-Stefan Description of Mixture Diffusion in Nanoporous Crystalline Materials. *Micropor. Mesopor. Mater.* **2014**, *185*, 30-50.
4. Krishna, R. Methodologies for Evaluation of Metal-Organic Frameworks in Separation Applications. *RSC Adv.* **2015**, *5*, 52269-52295.
5. Krishna, R. Screening Metal-Organic Frameworks for Mixture Separations in Fixed-Bed

Adsorbers using a Combined Selectivity/Capacity Metric. *RSC Adv.* **2017**, *7*, 35724-35737.

6. Krishna, R. Methodologies for Screening and Selection of Crystalline Microporous Materials in Mixture Separations. *Sep. Purif. Technol.* **2018**, *194*, 281-300.
7. Li, L.; Lin, R. B.; Krishna, R.; Li, H.; Xiang, S.; Wu, H.; Li, J.; Zhou, W.; Chen, B. Ethane/Ethylene Separation in a Metal-Organic Framework with Iron-Peroxo Sites. *Science*, **2018**, *362*, 443-446.
8. Lin, R. B.; Wu, H.; Li, L.; Tang, X. L.; Li, Z.; Gao, J.; Cui, H.; Zhou, W.; Chen, B. Boosting Ethane/Ethylene Separation within Isoreticular Ultramicroporous Metal-Organic Frameworks. *J. Am. Chem. Soc.* **2018**, *140*, 12940-12946.
9. Qazvini, O. T.; Babarao, R.; Shi, Z.-L.; Zhang, Y.-B.; Telfer, S. G. A Robust Ethane-Trapping Metal-Organic Framework with a High Capacity for Ethylene Purification. *J. Am. Chem. Soc.* **2019**, *141*, 5014-5020.
10. Chen, Y. W.; Qiao, Z. W.; Wu, H. X.; Lv, D. F.; Shi, R. F.; Xia, Q. B.; Zhou, J.; Li, Z. An Ethane-Trapping MOF PCN-250 for Highly Selective Adsorption of Ethane over Ethylene. *Chem. Eng. Sci.* **2018**, *175*, 110-117.
11. Lv, D.; Shi, R.; Chen, Y.; Wu, Y.; Wu, H.; Xi, H.; Xia, Q.; Li, Z. Selective Adsorption of Ethane over Ethylene in PCN-245: Impacts of Interpenetrated Adsorbent. *ACS Appl. Mater. Interfaces*, **2018**, *10*, 8366-8373.
12. Cai, J. F.; Yu, J. C.; Xu, H.; He, Y. B.; Duan, X.; Cui, Y. J.; Wu, C. D.; Chen, B. L.; Qian, G. D. A Doubly Interpenetrated Metal-Organic Framework with Open Metal Sites and Suitable Pore Sizes for Highly Selective Separation of Small Hydrocarbons at Room Temperature. *Cryst. Growth Des.* **2013**, *13*, 2094-2097.
13. Yuan, W. H.; Zhang, X. T.; Li, L. Synthesis of Zeolitic Imidazolate Framework-69 for Adsorption Separation of Ethane and Ethylene. *J. Solid State Chem.* **2017**, *251*, 198-203.
14. Liang, W. W.; Xu, F.; Zhou, X.; Xiao, J.; Xia, Q. B.; Li, Y. W.; Li, Z. Ethane Selective Adsorbent Ni(bdc)(ted)$_{0.5}$ with High Uptake and its Significance in Adsorption Separation of Ethane and Ethylene. *Chem. Eng. Sci.* **2016**, *148*, 275-281.
15. Chen, Y. W.; Wu, H. X.; Lv, D. F.; Shi, R. F.; Chen, Y.; Xia, Q. B.; Li, Z. Highly Adsorptive Separation of Ethane/Ethylene by an Ethane-Selective MOF MIL-142A. *Ind. Eng. Chem. Res.* **2018**, *57*, 4063-4069.

16. Liao, P. Q.; Zhang, W. X.; Zhang, J. P.; Chen, X. M. Efficient Purification of Ethene by an Ethane-Trapping Metal-Organic Framework. *Nat. Commun.* **2015**, *6*, 8697.
17. He, Y.; Zhang, Z.; Xiang, S.; Fronczek, F. R.; Krishna, R.; Chen, B. A Microporous Metal-Organic Framework for Highly Selective Separation of Acetylene, Ethylene, and Ethane from Methane at Room Temperature. *Chem.-Eur. J.* **2012**, *18*, 613-619.
18. He, Y.; Zhang, Z.; Xiang, S.; Fronczek, F. R.; Krishna, R.; Chen, B. A Robust Doubly Interpenetrated Metal-Organic Framework Constructed from a Novel Aromatic Tricarboxylate for Highly Selective Separation of Small Hydrocarbons. *Chem. Commun.* **2012**, *48*, 6493-6495.